UNCLASSIFIED

NATIONAL AERONAUTICS AND SPACE ADMINISTRATION

Space Programs Summary No. 37-34, Volume II

for the period May 1, 1965 to June 30, 1965

The Planetary–Interplanetary Program

(Title Unclassified)

UNCLASSIFIED
JPL - Letter to Authority NASA-Langley
on Nov. 4, 1970 signed by W. E. Hanson
Date: Jan. 4, 1971 By: R. Castain

JET PROPULSION LABORATORY
LIBRARY
SEP 13 1965
CALIFORNIA INSTITUTE OF TECHNOLOGY

Copy No. 480

JET PROPULSION LABORATORY
CALIFORNIA INSTITUTE OF TECHNOLOGY
PASADENA, CALIFORNIA

July 31, 1965

LAB B01468

GROUP 4 Downgraded at 3 ... Declassified after ...

UNCLASSIFIED

141020

Preface

The *Space Programs Summary* is a six-volume, bimonthly publication that documents the current project activities and supporting research and advanced development efforts conducted or managed by JPL for the NASA space exploration programs. The titles of all volumes of the *Space Programs Summary* are:

Vol. I. The Lunar Program (Confidential)

Vol. II. The Planetary–Interplanetary Program (Confidential)

Vol. III. The Deep Space Network (Unclassified)

Vol. IV. Supporting Research and Advanced Development (Unclassified)

Vol. V. Supporting Research and Advanced Development (Confidential)

Vol. VI. Space Exploration Programs and Space Sciences (Unclassified)

The *Space Programs Summary,* Vol. VI consists of an unclassified digest of appropriate material from Vols. I, II, and III; an original presentation of technical supporting activities, including engineering development of environmental-test facilities, and quality assurance and reliability; and a reprint of the space science instrumentation studies of Vols. I and II.

W. H. Pickering

W. H. Pickering, *Director*
Jet Propulsion Laboratory

Space Programs Summary No. 37-34, Volume II

Copyright © 1965, Jet Propulsion Laboratory, California Institute of Technology

Prepared under Contract No. NAS 7-100, National Aeronautics & Space Administration

This document contains information affecting the national defense of the United States, within the meaning of the Espionage Laws, Title 18, U.S.C., Sections 793 and 794, the transmission or revelation of which in any manner to an unauthorized person is prohibited by law.

UNCLASSIFIED

Contents

I. *Mariner* Mars 1964 Project 1

A. Introduction 1

B. Project Engineering 2

C. Systems 6

D. Telecommunications 7

E. Space Sciences 9

References 19

II. *Voyager* Project 20

A. Introduction 20

B. Spacecraft Design 21

C. Guidance and Control 34

References 38

III. Future Projects 39

UNCLASSIFIED

[redacted]NCLASSIFIED

I. *Mariner* Mars 1964 Project

A. Introduction

The early objective of the Planetary-Interplanetary Program is the initial probing of the planets Mars and Venus by unmanned spacecraft. The initial probing of Venus was successfully accomplished by *Mariner II*. The next step toward this objective is the initial probing of Mars by a *Mariner C* spacecraft.

The primary objective of the *Mariner C* mission (*Mariner* Mars 1964 Project) is to conduct close-up (flyby) scientific observations of the planet Mars during the 1964-1965 opportunity and to transmit the results of these observations back to Earth. The observations should, to the greatest practical extent, provide maximum information about Mars. Television, cosmic dust and a reasonable complement of field and particle experiments are carried. In addition, an Earth occultation experiment will provide data relating to the scale height and pressure in the atmosphere of Mars.

A secondary objective is to provide experience and knowledge about the performance of the basic engineering equipment of an attitude-stabilized flyby spacecraft during flight in space farther away from the Sun than the Earth. An additional secondary objective is to perform certain field and/or particle measurements in interplanetary space during the trip and in the vicinity of Mars.

The *Mariner III* (MC-2) spacecraft was launched on November 5, 1964. The nose cone failed to eject from the spacecraft thereby precluding solar panel deployment; the battery power was depleted 8 hr and 43 min after launch.

The *Mariner IV* (MC-3) spacecraft was successfully injected into a Mars encounter orbit about the Sun on November 28, 1964. The flight continues without significant change in any subsystem performance. The spacecraft is performing as designed and is continuously monitored by the world wide DSIF/SFOF.

The internal battery voltage continues to rise as time proceeds, and as this report period ends it is measured at about 36.8 v. The cause for this voltage rise is not known for certain, but it appears to be a result of one or two possible conditions

(1) a small trickle charge fed to the battery through a telemetric transducer, or

(2) a leakage of electrolyte in one or more cells.

[redacted]UNCLASSIFIED

The overcharge condition is not considered to be serious. However, the leakage or possible shorted cell could be disastrous if the spacecraft is ever required to go into a load sharing mode (required if the power demands exceed the solar panel capabilities). Because of this, all encounter planning will try to insure that a load sharing mode will not knowingly be required.

The solar plasma instrument data became unintelligible due to the normal lowering of internal temperatures which has an effect of increasing the voltage stepping recovery time constant, a condition brought about as a result of the failure experienced in this instrument in the first days of flight. When the failure occurred and the spacecraft was on the 33⅓ telemetry bit rate, the time between voltage measurement samples was not sufficient to allow discharging down to the next lower consecutive voltage step; this was partially corrected or compensated for when the bit rate was lowered to 8⅓ bits/sec. Now with the increasing time constant, resulting from the lowering temperatures, this condition was reached again.

Attitude control roll disturbances have occurred again after a long period (47 days) of no detectable perturbations. No loss of Canopus lock has been experienced during any of these.

The 3rd and 4th Canopus tracker field of view cone angle updates were observed without incident. This is the last of the internal commands generated by the CC&S to be experienced until MT-7, the encounter sequence start command.

Cosmic dust activity appeared to peak up in early May (3–4 per day) and since then has been settled out at a decreased average rate of between 1 and 2 per day. In addition, two or possibly three solar flares were detected by the spacecraft radiation and magnetic field instruments.

A series of radiation tests were performed on selected spacecraft subsystems in an attempt to determine their sensitivity to intense radiation fields. This was considered necessary as estimates of possible field strengths around Mars varied widely. Subsystems such as the Canopus tracker, data encoder, gyro electronics, scan system, television and planet sensors were tested and the results indicated that the spacecraft electronics appear to have a lower sensitivity limit of about 10^9 electrons. This figure is 2–3 orders of magnitude greater than the best estimates of the maximum Mars field intensities expected.

The plan for encounter has been agreed upon and intensive training and testing has taken place using the proof test model (PTM)/SFOF and SFO crews to enhance their ability to react in a careful and intelligent manner during the actual encounter, whether the encounter is a completely normal one or is perturbed by abnormal events. The plan to be followed on encounter will be to start the encounter sequence about two hours earlier than MT-7 and to pre-position the scan platform at an optimum scan angle for television pictures. Then back up ground commands will be sent to ensure starting and stopping of the tape recorder; these will be sent to arrive at the spacecraft shortly after the nominal narrow angle acquisition time (start of tape recorder) and after the 2nd end of tape signal from the tape recorder (stop the tape recorder).

A quarterly review was held at JPL on May 25, 26 by the NASA Headquarters *Mariner* Program Office where project status and particularly spacecraft performance was covered in detail. In addition, the thinking on encounter planning was covered; the evolution of the firm plan was continually discussed with the NASA Headquarters *Mariner* Program Manager since the quarterly review.

It has been decided to terminate all life test of *Mariner IV* subsystems as of July 31, 1965 and to stop PTM testing in support of the flight spacecraft by September 1, 1965, and to place it and its operational support equipment in storage with the MC-4 spacecraft by October 1, 1965.

B. Project Engineering

1. Selected Mariner IV Subsystem Electron Tests

a. Introduction. According to an estimate by Hugh R. Anderson[1] an upper bound on the electron flux to be encountered by *Mariner IV* at its closest approach to Mars can be estimated in several ways. Estimates range in magnitude from 3×10^4 electrons/cm^2 sec for electron energies greater than 0.23 Mev to an extreme upper limit of 1.2×10^{11} electrons/cm^2 sec ($E_e > 2$ Mev), with a more reasonable upper bound being about 10^8 electrons/cm^2 sec. There are many uncertainties in such

[1]Interoffice Memorandum, May 3, 1965.

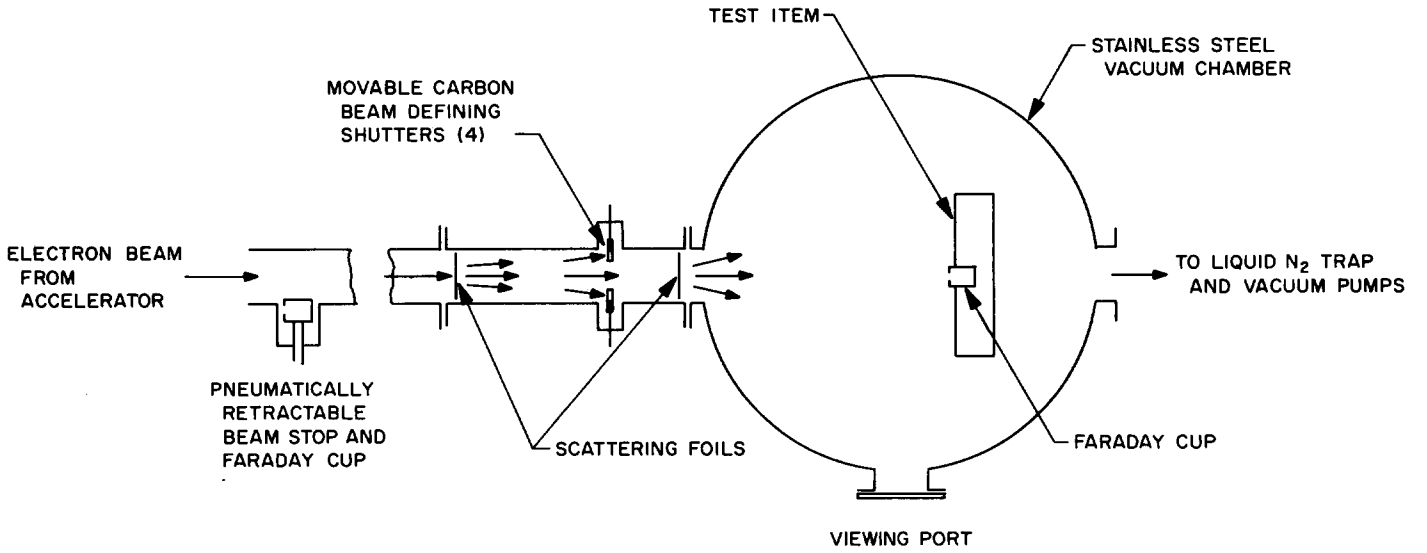
TEST ITEM
STAINLESS STEEL VACUUM CHAMBER
MOVABLE CARBON BEAM DEFINING SHUTTERS (4)
ELECTRON BEAM FROM ACCELERATOR
TO LIQUID N_2 TRAP AND VACUUM PUMPS
PNEUMATICALLY RETRACTABLE BEAM STOP AND FARADAY CUP
SCATTERING FOILS
FARADAY CUP
VIEWING PORT

Fig. 1. Test geometry

estimates, however; and a testing program was undertaken to assess *Mariner IV* susceptibility to electron radiation.

The subsystems which were tested and the corresponding minimum electron flux (electrons/cm² sec) seen to produce performance degradation are as follows: Canopus star tracker (2.5×10^9), data encoder (8×10^8), planetary scan platform (5×10^9), TV camera (5×10^9), narrow angle mars gate (6×10^9). The gyro and attitude control systems were also tested using a flux as high as 5×10^{10} but no degradation was observed.

b. Test set-up. The test was performed on the General Dynamics/Convair 3 Mev Dynamitron in San Diego. Fig. 1 shows the geometry of the test set-up. The electron beam from the accelerator may be stopped by the pneumatically operated Faraday cup allowing the beam current to be preset to the required test value. The scattering foils set 24 in. apart were used to broaden the beam spatially in order to cover the test item with a uniform electron flux. The four carbon shutters could be moved into or out of the beam to achieve a rough control over the beam attenuation. Vacuum in the chamber was maintained at 10^{-5} torr or below.

The shape of the beam after scattering was determined by driving a Faraday cup across the vacuum chamber with a screw mechanism while monitoring the collected current with an electrometer driving a strip chart recorder. Several flux maps obtained in this way are shown in Fig. 2 together with roughly fit Gaussian curves. The

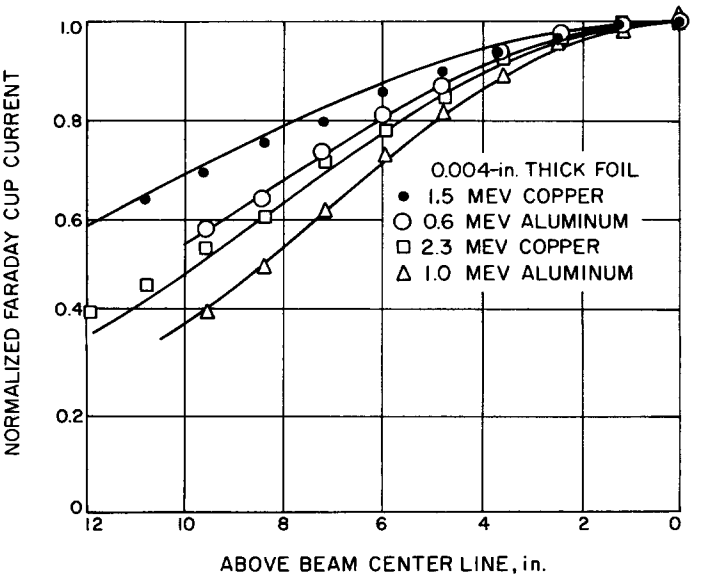

Fig. 2. Spatial distribution of scattered electron beam 26 in. from scattering foil

flux distribution was shown to be symmetrical about the beam center line by traverses below center, horizontally and at 45 deg from vertical. The curves were taken with one foil only in a traverse across the center of the vacuum chamber 26 in. from the foil. Similar curves were obtained by using two foils as shown in Fig. 1. It was found that changing the position of the carbon shutters did not change the curve shape, as far as it could be determined by our experimental accuracy.

It is apparent that the aluminum ($Z = 13$) foils are useful electron scatterers for this test only below 1 Mev.

Copper foils (Z = 29) were used for the higher energies. The lower Z foils were used whenever possible because the bremsstrahlung or x-ray production (as well as the scattering ability) rises as Z^2 (Ref. 1 Chap. 2).

Utilizing the test geometry described above, directly measurable beam fluxes attainable at the subsystem surfaces varied from 10^7 electrons/cm² sec to a maximum of 2×10^{11} electrons/cm² sec. The low fluxes were attainable only at lower electron energies where corona discharge inside the accelerator beam tube was not excessive. The upper flux limit is determined by accelerator stability at low energies and by the beam current that will burn a hole through the foils at higher energies. Electron energies from 0.5 to 2.6 Mev were used in the test. Flux monitoring was achieved by using a Faraday cup mounted adjacent to or on the front surface of the test item. The flux measurements are estimated to be accurate to ±20%. Electron energies referred to concerning test results are corrected for energy loss due to foil traversal, hence suffer from straggling induced energy spread. Taking into account the energy spread and the accuracy of the measured accelerator voltage the electron energies are accurate to roughly 10%.

The subsystems were mounted in their magnesium flight cases with the beam incident on the flight case. At the thinnest portions of the case the electrons had to penetrate about 0.552 g/cm² of magnesium to get into the electronics, thereby losing about 0.8 Mev. Note that the Canopus tracker, planetary scan preamplifier and motor, television preamplifier and optics, and the narrow angle mars gate are not protected by a flight case. A nominal 0.2 Mev electron energy loss occurs in penetrating the respective aluminum shields.

The test items were mounted on an adjustable aluminum pedestal and platform inside the vacuum chamber. With the exception of the planetary scan, television and narrow angle mars gate subsystems, the test items were located 39 in. from the last scattering foil. The above noted exceptions were mounted in the chamber center 26 in. from the foil in order to utilize external optical stimulus. The subsystems were connected by 35-ft cables to the OSE located outside the accelerator area.

c. Test procedure. Following exploratory test runs on the Canopus tracker to determine ballpark areas of malfunction the procedure was to initially irradiate the subsystem at 0.56 Mev for 20 min at a flux of 10^8 electron/cm² sec. This was chosen as a combination yielding a conservative simulation of radiation levels the spacecraft will experience during the encounter sequence. The program was then to increase the flux in approximately one-half order of magnitude steps (pausing at each level for subsystem checkout by the cognizant engineer), until a malfunction ensued or maximum accelerator flux was reached. The electron energy was then increased and the flux values again stepped through. Whenever a malfunction occurred the beam flux was adjusted downward in small steps in order to ascertain a threshold flux level for failure. The subsystem was also monitored after each malfunction to determine if permanent damage had occurred. This was done by moving the retractable beam stop in to intercept the beam. Subsystem recovery then gave evidence that RF fields, power line loading or other phenomena associated with operating the accelerator were not responsible for the observed behavior.

d. Results. Fig. 3 is a plot of the malfunction thresholds observed for the various subsystems. The various modes of failure are presented in Table 1. Note that the data encoder malfunctioned at electron energies which could not penetrate the flight case, indicating that bremsstrahlung produced by the electron decleration in the scattering foils and the flight case contributes significantly to the radiative system degradation. Such bremsstrahlung produced in the scattering foils acts to make this test more conservative. In any case the Mariner subsystems tested were found capable of functioning normally in the presence of estimated electron fluxes expected near Mars.

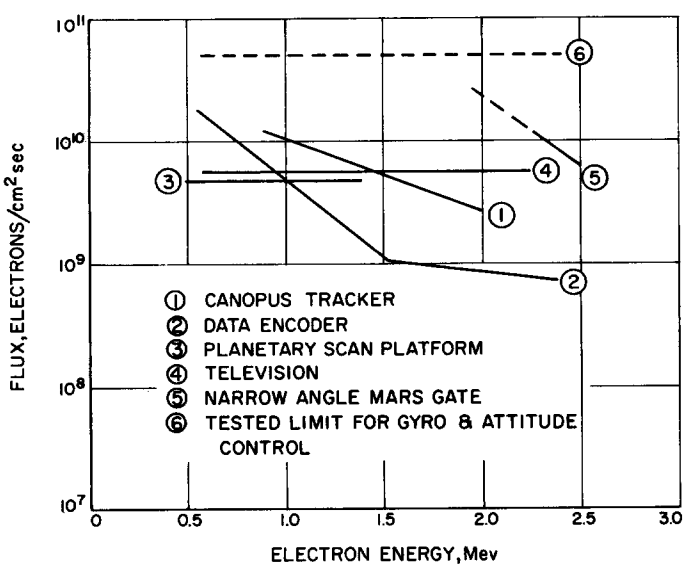

Fig. 3. Threshold malfunction levels

Table 1. Various failure modes

Subsystem	Radiation induced failure mode	Recovery
Canopus tracker	(1) Decrease in roll error saturation voltage below ±2.0 v (2) Null voltage offset (3) Apparent star intensity increase with no star in view	Star tracking ability was regained immediately following beam cut off. Front lens element was darkened, degrading transmission by 35% after an inferred total dose of 3000 rads
Data encoder	(1) Commutator sync loss predominant at energies below 1 Mev (2) Demodulation lock loss above 1 Mev (3) Event counter change of state (4) Switch from mode 1 to mode 4 at flux of 5×10^{10}	Immediate recovery following beam cut off
Planetary scan platform	(1) Unprogrammed scan direction reversals (2) Failure to generate planet in view signal (3) Failure to carry out programmed search mode	Recovery was achieved after about 20 min for medium flux levels. Up to 12 hr for flux levels of 10^{10}
Television	(1) White spots on the picture associated with transients on the video line (2) Switch to fast exposure speed (3) Increased noise level causing grayish backgrounds (4) Decrease in picture resolution	Recovery following high flux bombardments required about 20 to 30 min
Narrow angle Mars gate	False planet acquisition only at high energies and fluxes	Immediate recovery following beam cut off
Gyros and attitude control	No anomalous behavior found	

2. Launch Vehicle Integration: MC-4/Centaur Mission Study

On March 19, 1965 a presentation was made to NASA headquarters of potential uses of the *Mariner* MC-4 spacecraft. The JPL recommendations centered on a Mars mission in 1966–67.

In support of the study on which the recommendations were based, an investigation was conducted to determine the feasibility of using an *Atlas/Centaur* launch vehicle. The results of the investigation pertaining to the launch vehicle and its interfaces with the MC-4 spacecraft are summarized below.

Comparative studies of *Mariner* 1964 heliocentric trajectories with those available from *Centaur* in direct ascent modes for the 1966–67 Mars opportunity revealed that the (fixed) MC-4 high gain antenna would not continuously track the Earth. Long periods of radio silence would result. This difficulty with direct ascent trajectories for MC-4 was due to the large spread in planet arrival dates over the launch period. For this reason, therefore, the launch vehicle study was directed specifically toward *Centaur* vehicles having a restart capability for which heliocentric trajectories could be selected similar to those for *Mariner* 1964. Discussions were held with Lewis Research Center to explore the use of two-burn *Centaur* vehicles.

Launches of *Atlas/Centaurs* AC-12 and AC-13 were of initial interest because they are currently scheduled to bracket the Mars 1966–67 launch period, and the vehicles are to incorporate two-burn capability. Restart capability is to be qualified on the basis of two prior two-burn R&D flights. Because *Surveyor* launch operations activities are scheduled to be at a low level during the 1966–67 Mars opportunity, and because one of the two LC 36 A/B pads would be available for *Mariner* operations, it was concluded that a *Mariner* launch could be accommodated without impact on *Surveyor* schedules. A two-burn *Centaur* stage for *Mariner*, however, would have to be authorized early enough to have it ready in the fourth quarter of 1966. The pacing procurement item is the *Centaur* guidance system.

The spacecraft/launch vehicle interfaces examined included

(1) Clearances between the *Centaur* shroud and MC-4 spacecraft.
(2) Adaptability of the existing Lockheed Missiles and Space Co. *Mariner* 1964 adapter to mounting on the existing *Centaur* structure which extends forward of the tank.
(3) *Centaur* revalidation and turnaround time limitations, if any.
(4) Launch/hold constraints.
(5) *Centaur* telemetry available for spacecraft environmental measurements.
(6) Acoustic and vibrational environment of the spacecraft during ascent as compared to *Mariner* 1964.
(7) Extent of the launch period for a *Mariner* 1966-67 mission.

None of the factors listed above appear critical. The impact on the schedule, if any, of introducing an MC-4 matchmate and combined systems test in San Diego and of adding an additional two-burn *Centaur* to the program

was not determined. Procurement, manufacturing, test schedules, and costs were not studied. Within the scope of the study, however, the launching of MC-4 using *Atlas/Centaur* appeared feasible.

C. Systems

1. Mariner Mars 1964 Space Flight Operations

Mariner Mars 1964 Space Flight Operations (SFO) activities, covering the reporting period May and June 1965, have been directed toward planning, coordinating, and participating in encounter tests, flight operations for *Mariner IV* (MC-3) and generation of documents.

a. SFO encounter tests. A series of nine encounter tests were conducted using the *Mariner* Proof Test Model (PTM), simulated data, and the flight spacecraft as the data source. These encounter tests indoctrinated and exercised the SFO system operational and technical personnel in the system and procedures to be used during the Encounter Phase of the mission. The following is a list of tests and the number performed during May and June

(1) Encounter Alternate Plan (1 test)

(2) Encounter Backup Mode (4 tests)

(3) Encounter Scan Position (2 tests)

(4) Preliminary Readiness (1 test)

(5) Encounter–Operational Readiness (1 test)

b. Flight operations for Mariner IV (MC-3). Spacecraft performance during May and June were nominal, with the following standard (planned) and nonstandard events.

Standard (Planned) Events.

(1) Central Computer and Sequencer (CC&S) command MT-3 was issued May 7 at 14:27:17 GMT. This on-board command updated the Canopus cone angle from No. 2 to No. 3 set.

(2) The aluminum-silicone absorptivity standard temperature channel stepped May 11 at 05:43:15 GMT.

(3) CC&S cyclic Nos. 56 through 77 were observed on schedule, one every 66⅔ hr.

(4) CC&S command MT-4 was issued June 14 at 15:53:57 GMT to update the Canopus cone angle from No. 3 to No. 4 set.

Nonstandard Events.

(1) The spacecraft battery voltage continued to rise. A one data number increase was observed on each of the following days: May 4, 9, 16 and 24; June 3 and 15.

(2) The polished-aluminum absorptivity standard temperature channel stepped May 17 at 15:44:41 GMT, earlier than expected.

(3) Two solar flares were detected by spacecraft instruments, the first on May 25 at 23:00 GMT and the second on June 6 at 19:30 GMT.

(4) Disturbances in the roll channel of the Attitude Control Subsystem were observed June 9, 10, 11 and 16. No loss of Canopus occurred.

General. A major milestone was reached on May 4, 1965. *Mariner IV* passed the 132-million mile range from the Sun, where radio contact with the Russian Mars I probe ended in March 1963. As *Mariner IV* traveled past this point, it was sending back measurements from a region farther out from the Sun and Earth orbit than had been reached by any previous space mission.

c. SFO documents. *Mariner IV Progress Reports.* The purpose of the *Mariner IV* Progress Report is to present information on the performance of the *Mariner IV* (MC-3) spacecraft and to report, in general terms, the performance of the SFO System. Progress Report No. 3 covered the period of March 16, 1965 to April 30, 1965 (Launch + 109 days to Launch + 154 days) and was published June 7, 1965. Progress Report No. 4 will cover the period May 1, 1965 to May 31, 1965 (Launch + 155 days to Launch + 185 days) and will be published July 5, 1965.

Mariner Mars 1964 Technical Bulletins. The *Mariner* Mars 1964 Technical Bulletins are issued daily and report the daily status of the *Mariner* Mars 1964 mission. Technical Bulletins 154 through 214 were issued during May and June 1965.

Space Flight Operations Plan (EPD-122, Addendum I). This addendum describes the plan for the Encounter and Post-encounter period of the *Mariner* Mars 1964 Mission. Publication is scheduled for July 5, 1965.

Mission events flow diagram. The purpose of this diagram is to display all events, in flow diagram form that occur during the mission. Daily updating continues.

D. Telecommunications

1. Radio Subsystem

The radio subsystem aboard the *Mariner IV* spacecraft has operated continuously with no evidence of any malfunction or degradation of performance from the time of launch through this reporting period. The few anomalies that were observed are well understood and are reported in this article in the order that they were recorded. Before proceeding with the list, a brief description of the system is presented to acquaint the reader with the radio configuration. Fig. 4 is a simplified block diagram of the system. A more detailed description is presented in Ref. 2.

The system consists of a phase coherent transponder designed for maximum reliability through the independent use of redundant exciters and power amplifiers. A phase modulated RF signal may be either received or transmitted by the spacecraft on a directional antenna or low gain antenna, depending upon spacecraft orientation and operational mode. Diplexing of the signals on either antenna is accomplished through the use of circulator switches.

The received signal is coherently detected by means of a phase locked automatic phase control (APC) loop in the transponder receiver, the output being the modulated command subcarrier that is appropriately fed to the command subsystem for further processing.

When the transponder APC loop is in lock, the receiver local oscillator also serves as the transmitter frequency controlling element. When the APC loop is out of lock, transmitter frequency control is transferred to a fixed crystal oscillator. Thus, when the receiver APC loop is in lock, the signal transmitted from the spacecraft is translated in frequency and phase from the ground signal, but is coherent with it.

During the flight of the *Mariner* spacecraft several radio system anomalies have been noted.

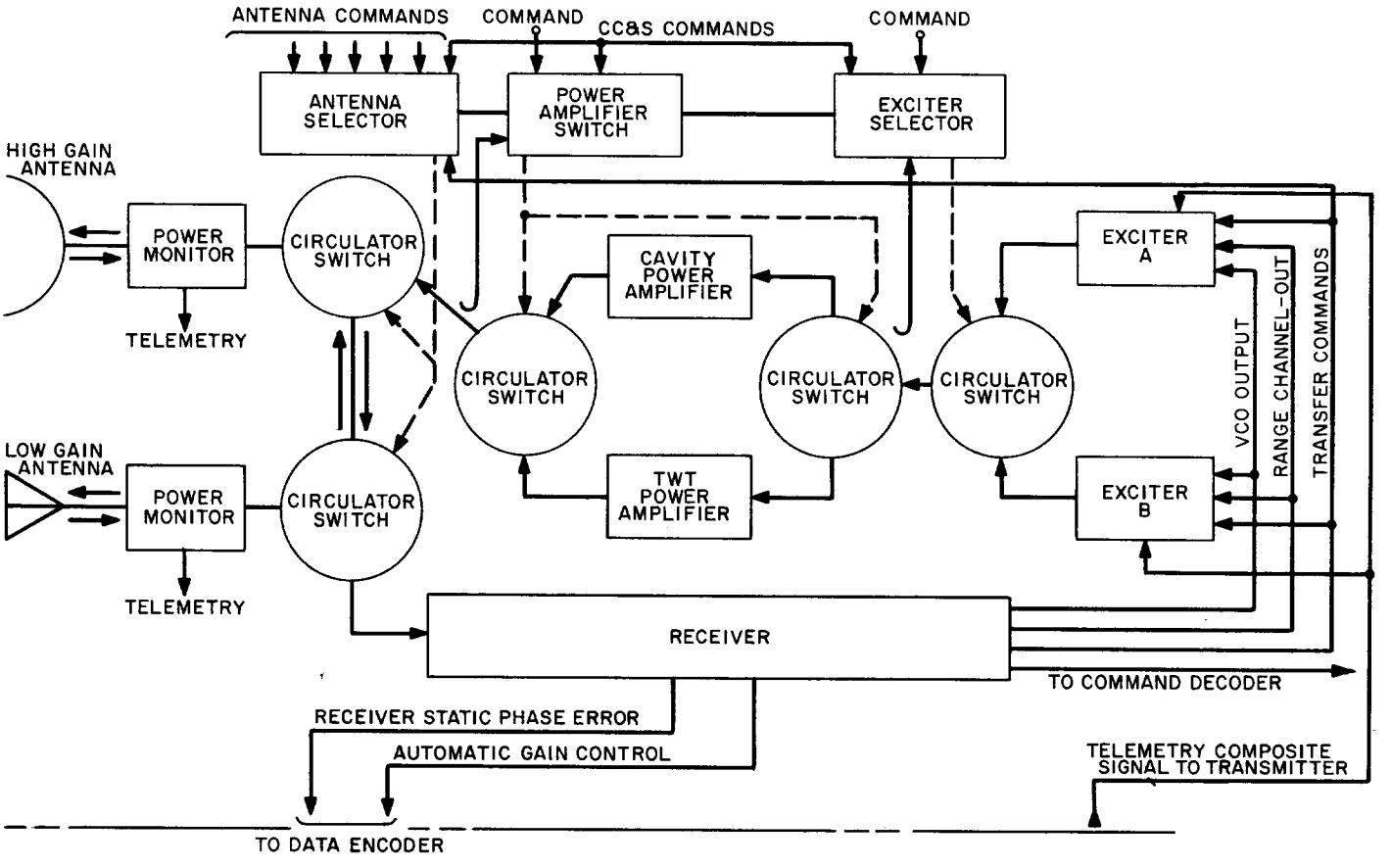

Fig. 4. Radio subsystem

a. Traveling wave tube (TWT) helix current variation. Following the power amplifier switch to the TWT amplifier by ground command on 1964 day 348, the TWT operated as expected, with one exception. Beginning of 1964 day 366, telemetry indicated that the TWT helix current was varying more than anticipated, and was generally tending to increase. It finally stabilized about 0.4 ma higher than the initial value. Discussions with the manufacturer indicated that helix current variation was a known characteristic of TWT's used in space applications and should be considered normal. Subsequent tests conducted at JPL with two TWT's from the same lot that *Mariner IV* is using confirmed this.

Continued observation of helix current since its stabilization value (about 7.7 ma) was reached has noted no further variation except those attributable to decreasing spacecraft temperature.

b. Interferometer effect. The interferometer effect is caused by mixing low and high gain antenna signals together and is observed as amplitude variations of the signal.

The high and low gain antennas are connected to the spacecraft receiver and transmitter by means of circulator switches. A characteristic of circulator switches is that they do not completely isolate one antenna from the other. For this reason, interferometer patterns predicted before launch are present when transmitting and/or receiving via the low gain antenna while the high gain antenna is pointing in the direction of Earth.

An equation for the interferometer antenna pattern based on the spacecraft configuration has been derived to aid in predicting spacecraft performance. The constants of the pattern equation were adjusted to fit the actual received carrier power curve.

When the transmitter was switched to the high gain antenna, a change in phase occurred of approximately 36 deg between the low gain antenna signal and the leakage signal from the high gain antenna. Also, the effective isolation between antennas changed from the 14 db value before the switch to 12.5 db after the switch. Since constructive or destructive interference is possible, depending upon amplitude and phase of the leakage signal relative to the amplitude and phase of desired signal via the low gain antenna, the spacecraft received signal strength, and the ground received signal strength changed at this time.

c. Frequency shift caused by central computer and sequencer (CC&S) CY-1 command. Both receivers at DSIF-42 dropped lock momentarily coincidental with CC&S CY-1 command on 1965 day 058. Since then, these transients have been observed almost every time while in one way lock. Analysis of the data indicated that this has occurred in one way lock since launch. Tests on the proof test model provided the following explanation:

(1) The CC&S switch closure changes the state of a flip flop (F-F).

(2) One of the dc power supplies for this F-F is common to the auxiliary oscillator.

(3) The F-F draws more current in one state than in the other.

(4) The voltage output of the dc power supply is slightly current dependent.

(5) The change in power supply voltage of approximately 10 mv causes a frequency shift in the voltage dependent auxiliary oscillator and results in about 30 cps frequency shift at the output S-band frequency.

When the spacecraft is in two way lock, the radio operates from the voltage controlled oscillator (VCO) which does not have a dc power supply in common with the current unbalanced F-F. Thus, the slight shift in frequency is not a failure, but a design characteristic. It was not observed during prelaunch system testing because sufficiently sensitive instrumentation to measure such small frequency changes is not part of a normal test configuration.

d. Best lock frequency investigation. The best lock frequency is the frequency onto which the spacecraft APC will lock in minimum time. It also corresponds to the average frequency at which the receiver VCO operates when out of lock. If this frequency is not known closely enough, DSIF may take a long time to acquire two-way lock.

Due to aging and temperature differences, the best lock frequency may change from the prelaunch value. For this reason, two methods have been proposed and are being used to continuously update the estimate of the best lock frequency.

The first method is the direct measurement, by DSIF, of the frequency giving the shortest lock-up time, and the only requirement is that the DSIF stations follow certain procedures to acquire two-way lock. The second method

consists of recording spacecraft static phase error (SPE) telemetric values when out of lock and then averaging the spacecraft SPE readings over a sufficiently long period of receiver out-of-lock condition. The average telemetric value can then be converted to spacecraft VCO frequency from the appropriate calibration table. Using the updated best lock frequencies, ground stations have repeatedly obtained two-way lock with the spacecraft within a few seconds after the signal arrives at the spacecraft. Prior to obtaining these data it occasionally took more than an hour to obtain two-way lock.

E. Space Sciences

1. Mariner IV Ion Chamber Failure Analysis

The *Mariner IV* ionization chamber performed nominally through the first 70 days of the mission. During this period, a profile of radiation intensity was faithfully recorded by the instrument as the spacecraft passed through each of the Van Allen belts, through the boundary of the magnetosphere, and into the relatively stable interplanetary region. Sixty-nine days after the mission began, a solar flare occurred. Both the ion chamber and the Geiger Müller (GM) tube recorded peak activity of the flare. As the flare subsided and the ion chamber returned to the normal background level, the GM tube indicated a slightly higher rate than expected over the downward trend, leveling off at a value approximately 30% above the expected preflare level. On the 84th day of the mission, after about 10 days of comparatively stable operation at this slightly anomalous level, the GM tube rate rose sharply from approximately 40 to 18,000 counts/sec, indicating a spontaneous, self-sustained discharge.

On the 109th day of the mission, the GM tube rate dropped to zero and the ion chamber interval became infinite. No response from either sensor has been observed since then.

It was calculated that the GM tube had first failed (by spontaneous discharge) after having counted $\sim 8 \times 10^8$ counts, after expending only 8% of its rated 10^{10} count life. In an attempt to understand this phenomenon, ten tubes were taken from the batch from which the flight tubes were selected. Seven tubes were operated at various fixed count rates until such time as each tube failed by continuous discharge. Three tubes were exposed to the higher flux levels, but without power applied. No significant shift in the voltage plateaus of these latter tubes was observed.

The tentative conclusion from the results obtained was that the total life-count of a tube depends upon the rate at which the tube counts; the higher the count rate the more counts a tube will assimilate before the onset of spontaneous discharge. Since each pulse is smaller at higher rates, it is likely that the tubes fail by spontaneous discharge after a certain amount of charge has passed through them. It also appears that the tube selected for *Mariner IV* may have been an especially short-lived tube in spite of the excellent stability displayed in selection and prelaunch tests. It appears that any other tube in the batch would have had a life-count capacity capable of completing the mission.

It was speculated that the quench gas, a mixture of chlorine and silicon-tetrafluoride, was depleted. This would explain the sustained count rate in the absence of sources. Good tubes and failed tubes were submitted to the Chemistry Section 326 for analysis and comparison. Analysis of the filling gas as performed by a mass spectrometer indicated no significant differences between gas from good tubes and gas from expended tubes. However, this test was deemed inconclusive due to the poor sensitivity of the available spectrometer. Gas samples have been submitted for further analysis and comparison on a spectrometer with improved sensitivity.

A darkening of the transparent cathode of the expired tubes was noted as they were allowed to operate in the spontaneous counting mode. Chemical analysis of cathode washings showed chlorine, one of the quenching gases, to be present on the cathodes of both good and expired tubes.

The most significant and entirely unexpected finding occurred when the tin-oxide cathode of a blackened tube was carefully scraped and the scrapings submitted to spectrographic analysis. Tests showed a remarkable 72% (by weight) tungsten content. The tungsten transport from anode to cathode is not yet fully understood.

The subsequent failure of the ion chamber portion of the instrument on the spacecraft, accompanied by the apparent simultaneous drop to zero in the GM tube rate indicated that perhaps the power supply, which is common to both detectors, had failed or had been shorted. This speculation was made more credible in view of the tungsten transport phenomenon. It was

hypothesized that the anode may have been steadily weakened by the emission of tungsten until electrostatic attraction by the cathode was sufficient to break the anode. The slender anode might be attracted to the cathode to the extent that physical contact might be made, the ensuing arc providing the energy necessary to weld the anode to the cathode, resulting essentially in a short-circuit of the power supply. In order to provide a method of quickly testing the hypothesis, it was necessary to sever the anode of the tube while the tube was counting normally under high voltage. To accomplish this, a good tube was mounted to the breadboard circuit. By means of optical lenses, the beam from a ruby laser was focused through the glass envelope of the tube onto the anode. With the tube in normal counting operation and powered by the breadboard ion chamber circuit, the laser was pulsed. The anode burned in two and the energized segment was attracted to the cathode. However, the anode did not weld to the cathode immediately, but required a period of approximately forty minutes, during which time the arcing between the electrodes was visible through the glass tube. Possibly the reason the welding was not instantaneous, but may have been instantaneous with the unit in space, was because burning the anode in half resulted in the formation of a small ball of tungsten on the melted ends of the anode. The additional mass, slightly larger than the diameter of the anode wire, might be expected to require considerably more energy for welding that an anode wire eroded to the breaking point by tungsten emission. Also, an eroded wire might have significantly less restoring force to counter the electrostatic attraction.

Additional evidence in favor of the shorted power supply hypothesis occurred when the life test unit failed in a manner much the same as the *Mariner IV* instrument. The GM tube output dropped to zero after a count rate profile and a time interval comparable to that of the spacecraft instrument. Simultaneously, the test voltages at all monitor points dropped in a manner that suggested a shorted supply. However, the ion chamber sensor continued to function with only slight increase in the expected period as opposed to the immediate failure of the chamber in space. This apparent discrepancy in the failure modes seems to have been resolved by subsequent tests on the breadboard circuit. If the power supply is shorted through the GM tube, breadboard tests indicate that the high voltage would decrease to a value below the ion chamber pulsing threshold if the life test unit (operating at ambient room temperature) were subjected to cold temperatures comparable to those experienced by the unit in space. It has been decided to await the end of the life test to verify this supposition, using the life test unit directly.

Further evidence for the postulated failure mode has recently been obtained. Three failed tubes functioning in their spontaneous discharge modes have successively been operated on the breadboard circiut until output from the tubes ceased. In all three cases when each tube finally quit producing the spontaneous output pulses, it was noted that the filaments had broken. In two of the tubes, the anode was observed to have been instantaneously welded to the cathode, resulting in a short-circuit of the power supply. The third tube proved to have an open circuit within the tube. This occurred because the break in the anode was so close to the glass feed-through sheath as to provide insufficient length for the energized end of the broken anode to reach the cathode.

In conclusion, there seems to be one bit of evidence that perhaps contradicts the proposed failure mode. Based on tests performed on the breadboard, it is calculated that if a short occurred in the GM tube as postulated, the energy dissipated by the instrument should increase by approximately 65%. Personnel from the thermal control area feel that such a step function increase in dissipated power would be detectable in the instrument's thermal performance. A review of thermal data from the instrument during the time in question does not indicate any obvious change in dissipated power. However, it is admitted that under certain conditions a power dissipation increase might be masked. Investigation using the life test unit after life tests are completed may resolve this question.

2. *Mariner IV* Plasma Probe Failure

a. Appearance of problem. The Massachusetts Institute of Technology (MIT) plasma probe operated normally at the fast step rate (33-1/3 bits/sec) for seven days after launch of the *Mariner IV* spacecraft. The instrument obtained many readings above the noise level and the plasma data continuously exhibited a clearly defined spectrum of one and, occasionally, two peaks. Instrument calibrations indicated proper operation without exception.

The instrument generates a high voltage which is variable in 32 steps from 56 to 10,000 v, but only those steps corresponding to 4210 and 5050 v are monitored by the high voltage calibration. On day 341 at 0000 hr, the high voltage calibration indicated high voltage failure by decreasing from normal to minimum over a 2 hr period. As the calibration readings neared minimum, the plasma readings decreased to the noise level of the instrument.

Other instrument calibrations appeared normal and justified the opinion that the problem was confined to the high voltage section.

It was immediately concluded that an arc had developed in the high voltage circuit and that there was insufficient high voltage to make plasma measurements. The existence of arcing was supported by evidence of system disturbance from day 341, 0200 hr to day 342, 0300 hr. Spacecraft data showed that data encoder deck skips occurred simultaneously with cosmic dust detector (CDD) hits. (There has been no evidence of a similar system transient since day 342.) The failure of R339 (Fig. 5) was considered and rejected. While the shorting of R339 would load down the high voltage, it would not necessarily produce RF noise, nor would it cause lower-than-normal high voltage calibrations. The opening of R339, a more likely mode of film resistor failure, would not lower the high voltage.

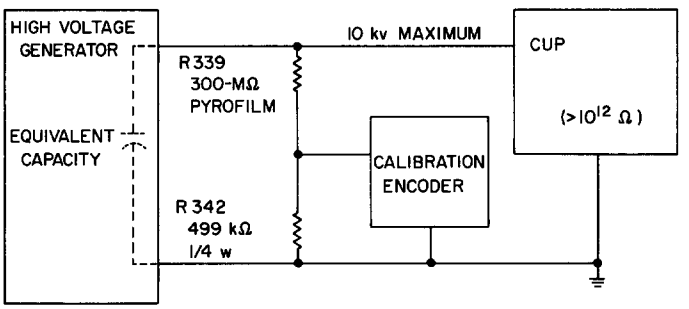

Fig. 5. Schematic of failed portion of instrument

b. Arc tests. The proof test model (PTM) probe was temporarily fitted with a spark gap during the last week of December. Bench operation showed that RF interference was being radiated directly and that it was present on the data readout line. When the instrument was mounted on the PTM spacecraft, data encoder deck skips and CDD hits were correlated with arcs at the spark gap. Thus, it was established that plasma probe arcing caused the system interference observed in the *Mariner IV* spacecraft.

c. Hypothesis. In a telephone conference of January 4, 1965, JPL was informed that a 300-MΩ resistor (R339) had opened in the MC-O life test being conducted at MIT. This information leads to the following hypothesis concerning the mode of failure:

(1) The opening of R339 would cause the high voltage calibration to decrease to minimum since the resistor is the top leg of a voltage divider feeding the calibration circuit (Fig. 5).

(2) As seen in Fig. 6, the high voltage consists of 80-msec bursts every 2.4 sec at the high-bit rate. The burst amplitude varies according to a preprogrammed pattern of 32 steps. At maximum output, there is a 2-kv p-p 2-kc square wave superimposed on 9-kv dc. At less than maximum output, the burst amplitude is less but the ratio of ac to dc is constant. At the end of the burst, the ac terminates abruptly but the dc is stored in the capacitors of the high voltage generator and must discharge through R339 and R342 (Fig. 5). In the first burst of Fig. 6, the instrument would be measuring all plasma with an energy level lying between 8 and

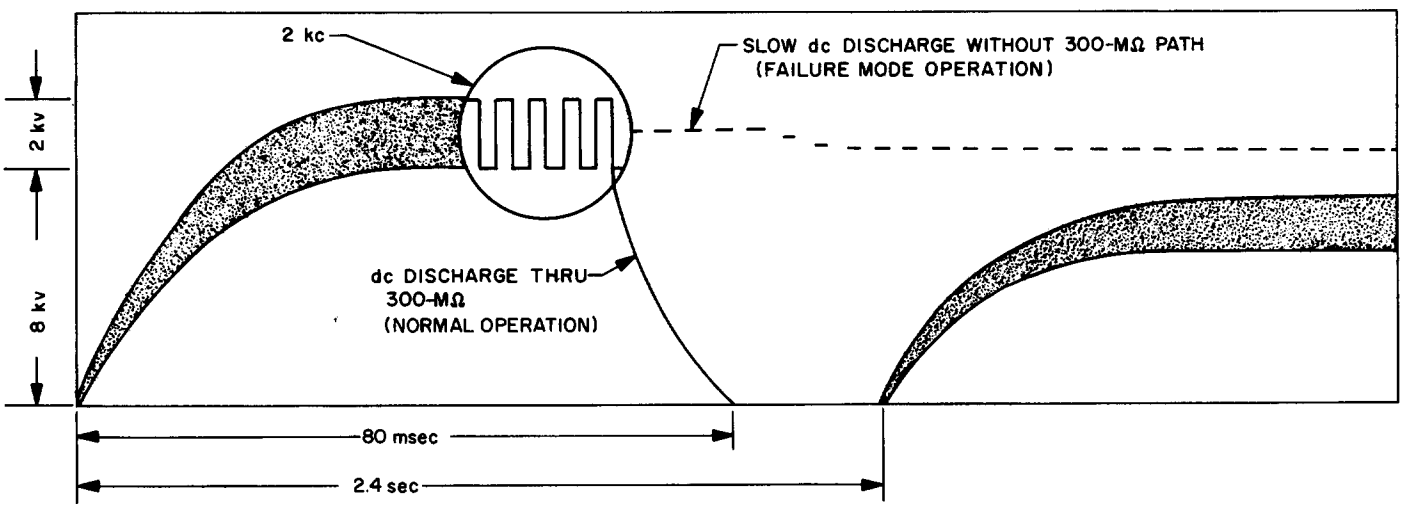

Fig. 6. Normal and failed high voltage waveforms

10 kv. It is important to note that the instrument does not sense plasma lying outside the ac envelope and that high dc potentials permit only high energy plasma to be seen.

The opening of R339 would open the dc discharge path and result in the slow decay rate which is illustrated by the dashed lines in Figs. 6 and 7(a). Although the instrument would still go through its sequence of steps, the dc level would no longer follow the proper pattern but would remain high and permit only the higher energy plasma to be seen. Furthermore, the calibration of the instrument would vary from step to step because the ac to dc ratio varies with each step. Therefore, the instrument sensitivity is reduced on all but the highest voltage step.

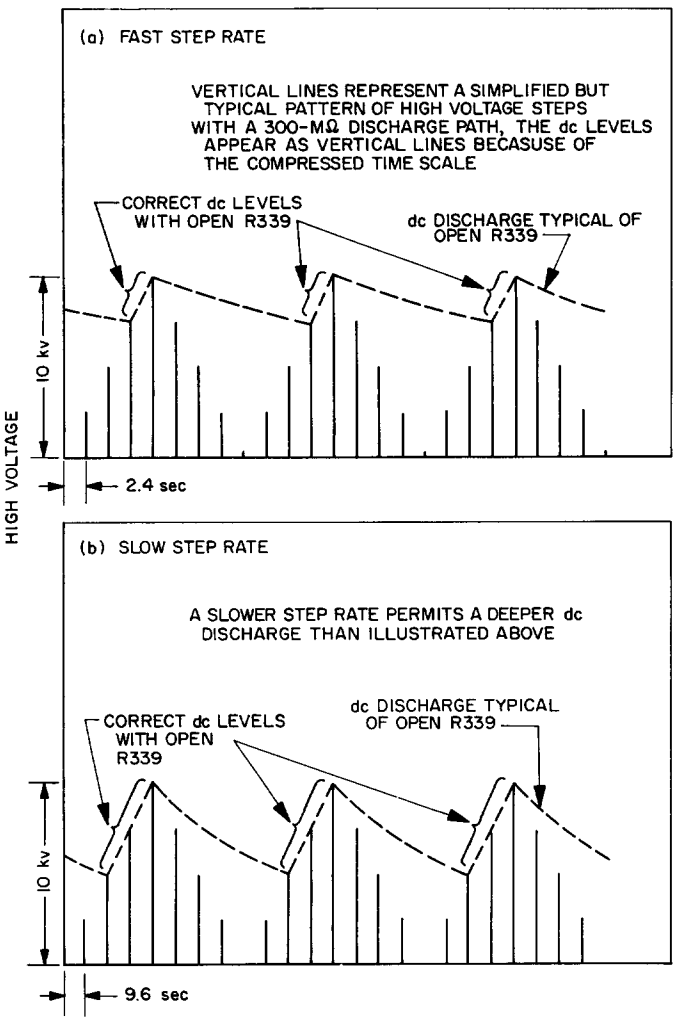
(a) FAST STEP RATE
VERTICAL LINES REPRESENT A SIMPLIFIED BUT TYPICAL PATTERN OF HIGH VOLTAGE STEPS WITH A 300-MΩ DISCHARGE PATH, THE dc LEVELS APPEAR AS VERTICAL LINES BECASUSE OF THE COMPRESSED TIME SCALE
CORRECT dc LEVELS WITH OPEN R339
dc DISCHARGE TYPICAL OF OPEN R339
10 kv
2.4 sec
HIGH VOLTAGE
(b) SLOW STEP RATE
A SLOWER STEP RATE PERMITS A DEEPER dc DISCHARGE THAN ILLUSTRATED ABOVE
CORRECT dc LEVELS WITH OPEN R339
dc DISCHARGE TYPICAL OF OPEN R339
10 kv
9.6 sec

Fig. 7. The effect of failure on spectral analysis (a) effect at 33-1/3 bits/sec sampling rate (b) effect at 8-1/3 bits/sec sampling rate

(3) The opening of R339 could result in arcing either within failed resistor or in some other part of the high voltage circuit. The tendancy to arc externally would be increased by the presence of voltages which are slightly higher than normal and which are maintained at high levels for much longer periods. It is known that arcing will occur under normal conditions if the high voltage generator is operated without the several picofarads of load capacitance presented by the cup.

d. Support of hypothesis. At first, MIT doubted that the opening of R339 was a likely cause of the *Mariner IV* plasma failure; it was felt that there would be enough leakage, especially in the back direction through the high voltage rectifiers, to provide an adequate discharge path for the dc. Subsequent tests at MIT and JPL proved that the presence of the resistor was necessary to provide an adequate discharge path, and that without the resistor the dashed discharge curves of Figs. 6 and 7(a) would result. An examination of the MIT life test data revealed that R339 failed over a period of 6 hr in the life test at MIT. R339 was also found to be open in the PTM probe at JPL. The date of this failure is entirely unknown since the PTM is the one model which does not incorporate a high voltage calibration in accordance with engineering change request, (ECR) 6930. Without the incorporation of the ECR, no normal bench or systems test would indicate the failure of the resistor. All personnel associated with the plasma probe now concur that the MC-3 failure is undoubtedly due to the opening of R339.

The failure of R339 is still the only phenomenon which can explain an anomaly found in the *Mariner IV* spacecraft data. Since December 6, 1964, *Mariner IV* data indicate that plasma is still occasionally measured, but only as the plasma steps are ascending. As seen in Fig. 7(a), the vertical lines represent the desired dc waveform for each high voltage burst. The opening of R339 causes the dc potential to follow the dashed line. As a result of the slow decay, the dc voltage is correct for only a few ascending steps. Since the ac and dc levels are correct for these bursts, the instrument will properly measure any plasma present in the corresponding energy levels. Little plasma will be seen in the remaining steps because the narrow ac window makes the instrument insensitive and the high dc potential limits the measurements to high energy plasma, which at present is relatively scarce.

A slower step rate will permit a deeper dc discharge as shown in Fig. 7(b). With a deeper dc discharge, the correct voltages are established for a greater number of energy steps. Not only will there be a greater number

of correct measurements, but measurements will be made at low energy levels where more plasma has been seen. When the step rate was reduced on day 3, the *Mariner IV* spacecraft data showed an increase in plasma activity as predicted.

Since the dc discharge curve is established primarily by the leakage of the high voltage rectifiers, it varies greatly with temperature. In recent months, cooler instrument temperatures have reduced the rate of discharge to the point where very little plasma can be seen.

DC discharge curves have been run at JPL and MIT on the remaining plasma probes as instrument availability permitted. Since there is no reason to assume that the *Mariner IV* curve is atypical, a probable curve can be synthesized and used to recover some of the plasma information which came through from the defective instrument before cooler temperatures prevailed. An absolute calibration of the *Mariner IV* instrument will never be possible because the contributing parameters vary significantly from instrument to instrument.

The Pyrofilm Resistor Company, manufacturer of R339, states that it is the presence of a radial ac field which causes resistor failure and that, furthermore, failure would be expected with the intensity of the field produced by the 2-kv burst. In the laboratory, it was observed that the field produced ionization within the resistor and gradually removed the carbon-film resistive element from its ceramic base. It is to be noted that the flight resistors successfully passed a screening procedure. Unfortunately, this procedure did not subject them to an ac stress.

3. *Mariner IV* Television Interpretation Studies

In the period between launch and the return of TV picture data, members of the scientific team responsible for evaluation of the pictures are becoming familiarized with the abilities and limitations of the spacecraft television system as compared with standard Earth and Earth-satellite based TV, and photo-reconnaissance devices. The problem of interpreting an unknown planetary surface has led to laboratory and field tests to provide the specialized photointerpretive data necessary to more precisely evaluate the encounter photographs.

The original proposal to do TV photography of local terrain from elevated ground sites and/or aircraft was discarded in favor of laboratory studies as the magnitude of the problem was more fully understood. The pre-encounter activities were divided into five general categories

(1) A television system was selected that would closely simulate the flight system (S/N MC-4) in sensitivity, color response, and geometric characteristics. The system selected was a hybrid consisting of electronics from the prototype system and a proof test model (PTM) camera-head of an early mechanical design with especially selected vidicon tube and color filters of the flight type. This system (S/N P-2) exhibits response characteristics within a few percent of the flight system (Fig. 8).

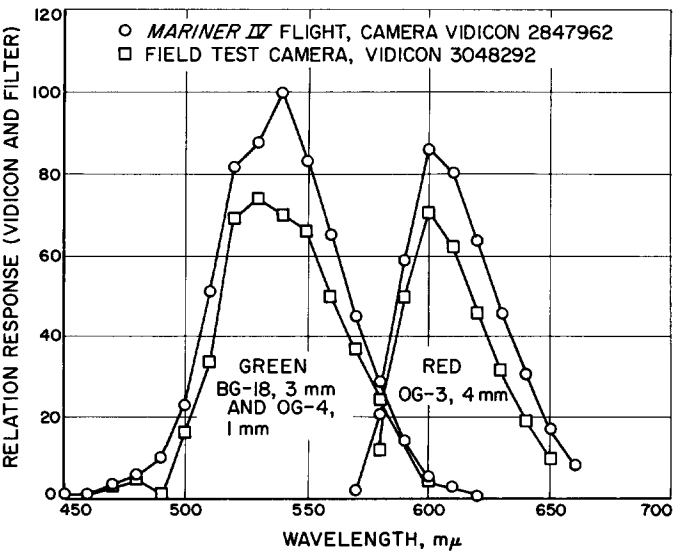

Fig. 8. Spectral response of flight and field test TV camera systems

(2) *Laboratory tests* will be performed to determine detectability thresholds of simple simulated topographical features (e.g., slopes and edges, characteristic of faults and mountain-forming activities; and variations in color and albedo typical of terrain of differing composition or age lying adjacent. Combinations of both phenomena will also be studied.

Quantitative testing was done with simple step models painted in grey shades to simulate Martian light and dark area albedos ($\rho = 0.18$ and 0.07, respectively). The models were illuminated by collimated light at geometries analogous to those anticipated at encounter. A 750-w spotlight beam folded by an 88% reflecting mirror provided the light. The models were mounted on a three degree-of-freedom

pedestal and oriented to desired positions relative to the TV camera and the light beam (Fig. 9).

Additional subjective evaluation studies were made using U. S. Army Map Service topographical relief maps painted in suitable colors to simulate terrain as seen from high altitudes (Fig. 10).

(3) *Field operations at the Mt. Wilson Observatory* took place during the March 1965 opposition in order that the sensitivity settings and the color filter selections might be checked by photography of the actual planet. The TV system was coupled to a photometer scanner on the 60-in. telescope in a folded Cassegrain configuration and direct TV photos were taken of Mars. To compensate for the difference in optics (the flight telescope is a 12-in. focal length telescope, T/8; the 60-in. telescope Cassegrain focus is f/22) variable exposure time was added to the TV and most pictures were taken at 800 msec. On the nights of March 19–20, 1965, when reasonable seeing (4 to 6) and very good atmospheric transparency were experienced, more than sixty pictures of Mars (Fig. 11) were obtained and the video signals recorded on magnetic tape. Subsequently, the data were digitized, played back into the PDP-4 computer, and 35-mm negatives were obtained from the link video processor for analysis.

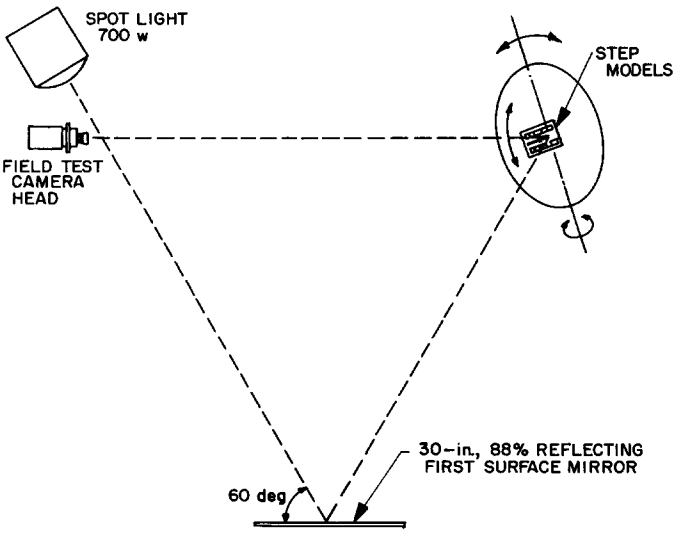

Fig. 9. Laboratory set-up for model studies

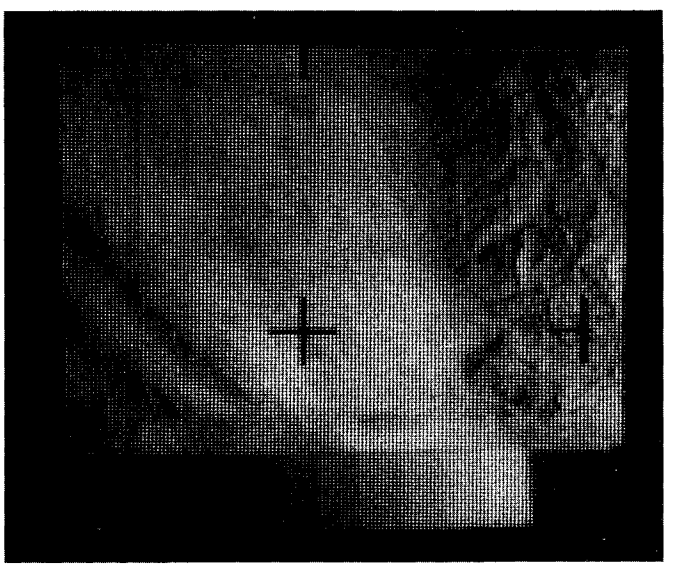

Fig. 10. Terrain model of the Bakersfield, California area. Also shown is the linear grey step chart providing a check of system gamma during model studies

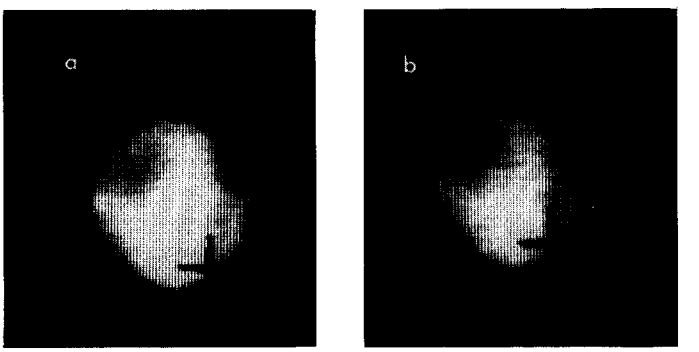

Fig. 11. Mars viewed from Mt. Wilson (a) green filter (b) red filter

(4) Optimized data and picture processing techniques will be employed. Encounter pictures will be received in six-bit digital form. After being decoded by computer, these will be processed by the Link recorder at the telemetry processing station onto 35-mm film. The film is exposed by a CRT beam that is intensity modulated by a voltage proportional to the digital level as it scans a 200×200 element format.

Laboratory and field test TV picture data are recorded on magnetic tape and by a Flight Research Corporation time lapse ciné recording of the TV monitor display. The magnetic tape data are digitized during playback and after suitable computer conditioning are processed by the TPS Link system in the same manner as spacecraft data.

To enhance the interpretability of encounter pictures, various parameters of the Link system operation and the computer processing have been varied. The basic 200 × 200 element raster leaves large spaces between dots on the picture [Fig. 12(a)]. To provide a smoother appearing picture, the raster size was decreased and the dots (CRT electron beam) defocused slightly. Additional fill-in will be accomplished by polynomial interpolation between picture elements to expand the picture to a 400 × 400 raster. To ensure that all of the data in the picture can be seen, the computer can invert all data so that the Link system may operate in a more linear region, and the Link gamma will be adjusted to provide a lower but more linear brightness spread (i.e., $\gamma = 1.0$, cf. $\gamma = 1.5$). The result is a picture showing the scene as photographed; that is, as continuous data, without loss of the information between dots as found with the original processing technique [Fig. 12(b)].

(5) Public Information Office (PIO) Activities consisted of providing for PIO release, *Mariner* TV camera pictures of photographs taken by the TIROS and *Ranger* spacecraft. Additionally, pictures of a topographical map of Southern California were taken. In each case, resolution of features in the pictures was arranged to approximate a *Mariner IV* view at the fly-by distances predicted for encounter.

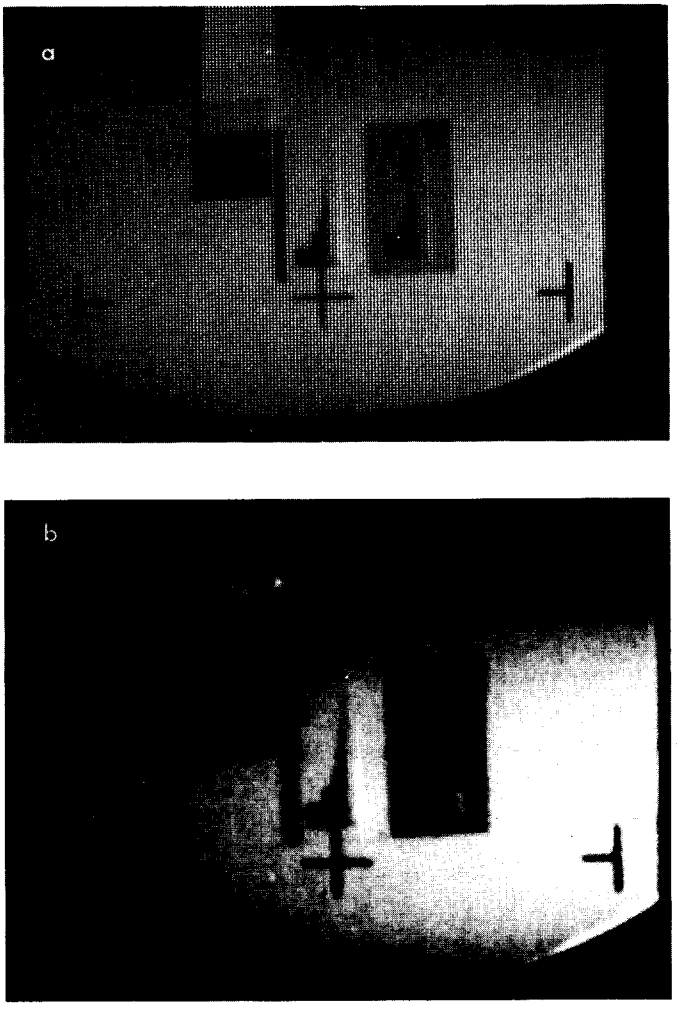

Fig. 12. Link system processed model study picture (a) normal operation, (b) optimized to *Mariner* TV operational parameters

Subsequent to encounter, it is anticipated that the model studies will continue to further refine the interpretation of the TV pictures of Mars. Planning is proceeding toward data synthesis in the opposite direction as heretofore; i.e., based on observed data, models will be fabricated and photographed in an attempt to simulate Martian surface phenomena. If portable instrumentation is available, particularly magnetic tape recording equipment, aerial surveys will be conducted to try to match terrestrial surface formations, and rock and soil materials to those observed on Mars.

4. Spurious TV-Image Phenomena

a. Introduction. A brief study has been made of a spurious image phenomena that arose in the latter stages of the development of the *Mariner* TV camera-head. The general appearance of the phenomena is illustrated in Fig. 13 where it will be noted that a dark line appears at the top of the picture.

The spurious line first became evident when a revised optics assembly required readjustment of the vidicon focus position. The cause was determined to be interaction of the shutter solenoid field with the vidicon photoconductor. Fig. 14 is a photograph of the front end assembly showing the relative positions of the solenoid and vidicon. Added shielding would remove the problem. The image defect was not sufficiently adverse to warrant possible schedule delays for implementing reliable shielding hardware.

There are two possible explanations for the origin of the line. The first assumes that it is a position phenomena that corresponds to a particular orientation of the solenoid magnetic field. The second assumes that it is a time phenomena that is related to magnetically induced particle-relaxation times in the semiconductor crystal lattice.

UNCLASSIFIED

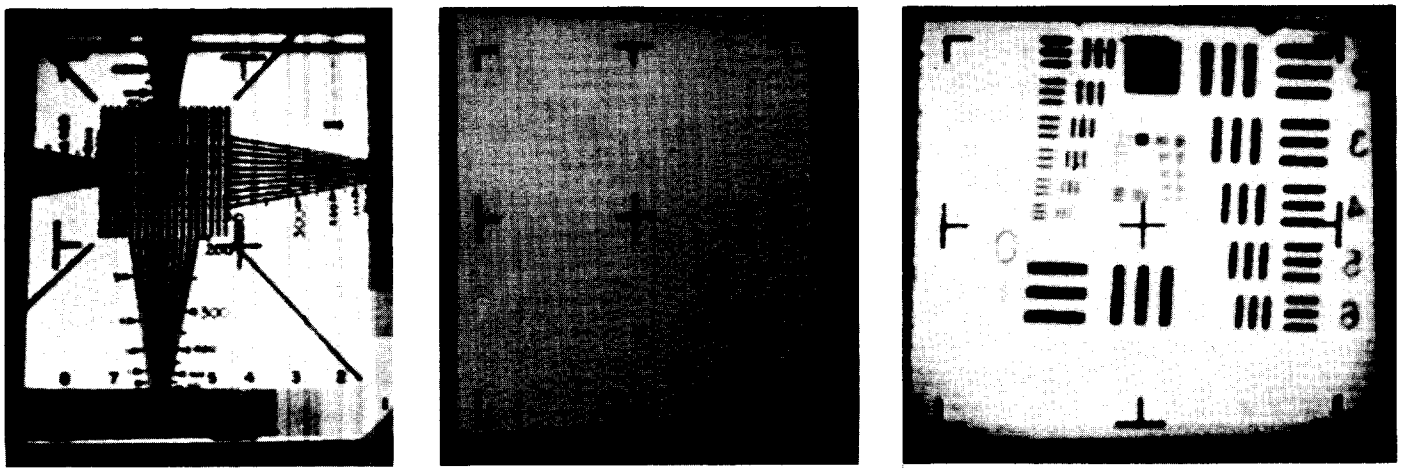

Fig. 13. Spurious line phenomena in *Mariner* TV system

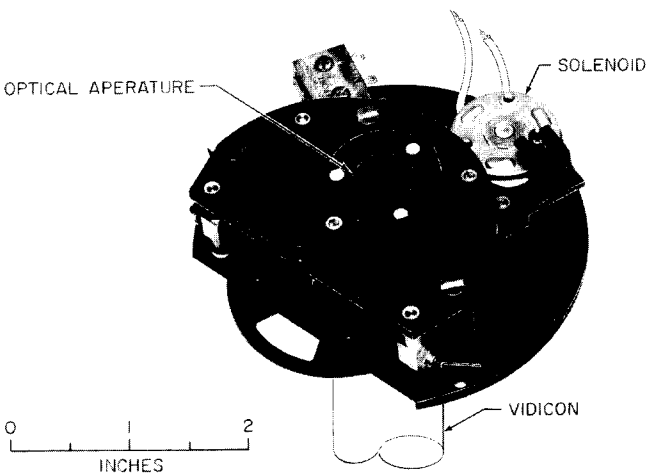

Fig. 14. Camera head shutter assembly

b. Vidicon operation. Before discussing either possibility, the operation of the slow-scan vidicon will be described together with certain observations that have been made. Prior to exposure, the vidicon is in an erase-and-prepare mode. During this time, the capacitive component ΔC of the picture elements is charged by the scanning-beam to the applied target potential. This sets up an electric field normal to the semi-conductor surface. Subsequent exposure generates mobile carriers that create a displacement current i that is oriented by the electric field to discharge the ΔC elements. In the read-out mode that starts coincidentally with exposure, the scanning-beam replaces the ΔC charge to produce the signal-current. In *Mariner*, the signal-current is an RF modulated component at 105 kc that is produced by chopping the beam. Two hundred lines are scanned out in a frame period of 24 sec with an active line time of 14.4 msec and an over-all line time of 120 msec.

c. Magnetic-field interaction. The exposure is electromechanically timed with a two-pulse open-close shutter action. Two exposure times are provided, 200 and 80 msec, with a drive-pulse width of 25 msec. Only the trailing edge of the first pulse and the leading edge of the second pulse are included within the optical exposure. Thus, while the photoconductor is illuminated, there are two switched magnetic fields, one in either direction. The spurious line becomes evident during the subsequent read-out period at times which may be 1 or 2 secs later than the exposure time. The pulsed-field magnitude measured in the vicinity of the vidicon faceplate is 2 gauss. The phenomena under discussion is most evident when the exposure operates with the 200-msec pulse spacing as shown in Fig. 13. The effect is less pronounced and occurs earlier in the read-out scan with the 80-msec spacing.

Attempts have been made to create spurious delayed images by introducing into the illuminated photoconductor changing magnetic fields produced by switched solenoids or hand-moved magnets. These are at best only marginally noticeable, probably because of timing difficulties. If the same fields are applied during the later read-out mode, the visible effect produced occurs only at the instant signal current is being produced, i.e., Faraday's law.

If the spurious image is to be caused by a positional phenomena, then some critical value and direction of a magnetic-field line must disturb the electrical field in the ΔC elements concerned at the time of exposure. Such an event might be produced by the Hall effect.

UNCLASSIFIED

d. The Hall effect. In 1879, E. H. Hall discovered that a potential difference arose perpendicular to the direction of current flow when a suitably oriented magnetic field was introduced into a material carrying current. It was not until 1934 that the Hall effect was first noted in photoconductors when it was then described as the PEM or photoelectromagnetic effect. The PEM effect is described as follows: If a semiconductor is illuminated, and a magnetic field introduced perpendicular to the direction of illumination, an emf is induced that is normal both to the photocurrent and the magnetic field.

The relationship between the magnetic field of the solenoid and the photoconductor in the *Mariner* camera-head is illustrated in Fig. 15. The coordinates are shown more simply in Fig. 16(a)

where

H represents the solenoid field

E_x the direction of the electric field across the semiconductor

E_h the field induced by PEM.

Illumination is directed along the x-axis and generates a photocurrent i.

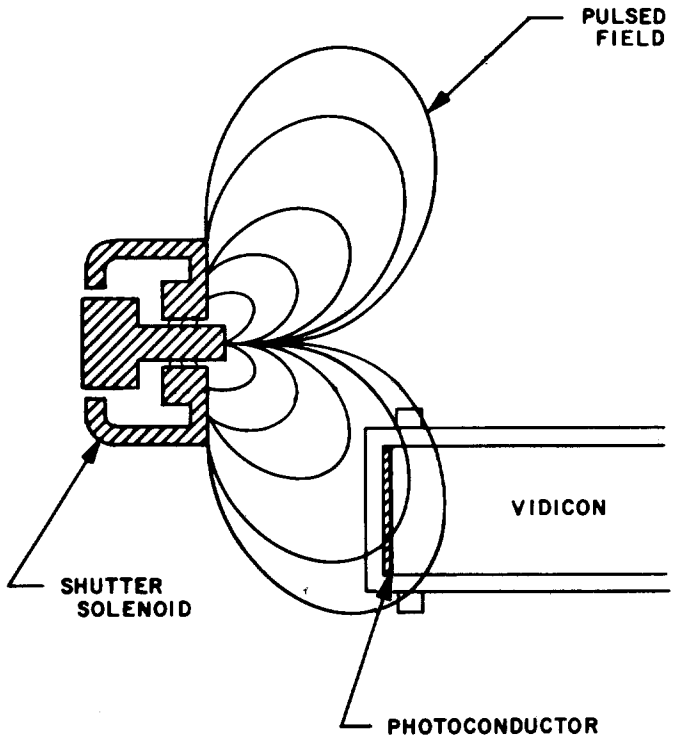

Fig. 15. Relationship of photoconductor to shutter-solenoid field

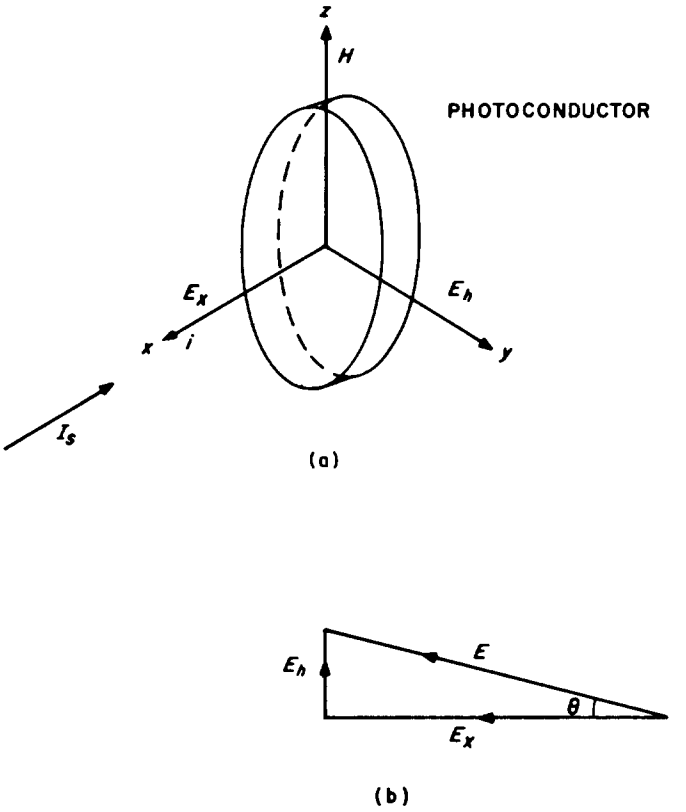

Fig. 16. Reorientation of the electric field across the crystal lattice with an added magnetic field

In accordance with a simplified analysis presented by R. H. Bube (Ref. 3), the potential that produces E_h is proportional to the current density j and the magnetic-field intensity H, i.e.,

$$\text{Grad } V_h = -h(j \times H) = -hjH = -E_h, \qquad (1)$$

where h is the Hall constant. As shown in Fig. 16(b), the resultant electric field may be regarded as a change in the direction of the original field E_x operating in the crystal lattice. The change in the direction is the Hall angle,

$$\tan\theta \approx \theta = E_h/E_x = hjH/j/\sigma = Hh\sigma \qquad (2)$$

where σ = the conductivity.

By considering the magnetic and electric forces acting on the electron in the y-direction, it can be shown that $E_h = jH/ne$ where n = the free carriers produced by illumination and e is the electron charge. Substituting in Eq. (1) the Hall constant $h = 1/ne$ the Hall angle $\theta = H/ne\rho$, where ρ is now the target resistivity.

The Hall angle may be determined for the *Mariner* vidicon by considering an elemental picture area ΔA and

estimating the population n from the quantum efficiency. A typical value for the *Mariner* vidicon is $n = 0.44 \times 10^6$ photoelectrons for an illumination $I_s = 0.01$ ft-c/sec. Taking $\rho = 0.5 \times 10^{14}$ ohm/cm^3, $h = 1/(0.44 \times 10^6 \times 1.6 \times 10^{-19}) = 1.4 \times 10^{13}$. The Hall angle $\theta = (1.4 \times 10^{13} \times 2.0)/(0.5 \times 10^{14}) = 0.56$ rad $= 32$ deg for a measured solenoid/field at the photoconductor $H = 2$ gauss.

This brief analysis appears to indicate that the magnitude of the solenoid field is sufficient to produce appreciable disorientation of the normal electric field across an ΔC element.

e. Spin-resonance. Considering next a time phenomena as the origin of the spurious image, a disturbance in the photoconductor crystal lattice that is produced in the time domain requires a relaxation phenomena of an oscillatory form in order to meet the nature of the observed line image, which when sloped appears and disappears on succeeding lines. This might be expected from nuclear particle spin-resonance activated by a fast-changing magnetic field operating in the presence of an RF current, the 105-kc beam-current component.

The energy equation for nuclear resonance,

$$h\nu = g_l B_N H \tag{3}$$

where $h = 6.6 \times 10^{-27}$ ergs/sec, $\nu =$ the RF frequency, B_N is the nuclear magneton, g_l is a factor related to the gyromagnetic ratio. For proton resonance, $H = 2.35 \times 10^{-4} \cdot \nu$ so that for $\nu = 105$ kc, $H = 25$ gauss, which is much higher than the field measured.

Similarly, for electron resonance,

$$h\nu = gBH \tag{4}$$

from which $H = 3.57 \times 10^{-7} \cdot \nu$ and for $\nu = 105$ kc, $H = 0.04$ gauss, much lower than the measured field.

Electron spin-resonance has been studied in semiconductors but relaxation times are extremely fast. Nuclear-resonance relaxation times on the other hand are of the order of that experienced during the vidicon readout time, 1 sec or longer. It is possible that an oscillatory nature to the spin-resonance would be observed on a sensitive system such as represented by the *Mariner* camera system, while remaining unnoticed by previous experimenters.

f. Conclusion. Of the two causes of the phenomena investigated the Hall effect seems to be the more likely origin of the spurious line. The Hall voltage depends inversely on the number of carriers and the thickness of the semiconductor. The slow-scan vidicon photoconductor is only a few microns thick and the displacement current only a few nanoamperes.

5. Space Sciences Encounter Planning Activities

a. Introduction. Space sciences personnel have been preparing for the *Mariner IV* encounter with Mars. Early in May 1965, an encounter planning group, staffed by cognizant project personnel from the space sciences analysis and command (SSAC) group and chaired by the division project representative, was created to define division requirements in encounter operations, establish tasks to meet such requirements and appoint cognizant persons to perform the tasks. The group supports the project encounter preparations working group (EPWG), chaired by the spacecraft project engineer, and refines the broader requirements of the EPWG and translates them to a detailed division effort.

In support of these groups, specialized auxiliary monitoring equipment has been installed in the space flight operations facility (SFOF) and personnel have participated in encounter preparation tests at SFOF, the spacecraft assembly facility (SAF) and in special subsystem tests.

b. SSAC encounter planning group. The group is organized into three subgroups and an SSAC council. The council acts in an advisory capacity; the three subgroups are

(1) the cognizant engineers, cognizant scientists and investigators associated with the cosmic ray telescope, cosmic dust detector, trapped radiation detector, ionization chamber, plasma probe and magnetometer,

(2) science subsystem project personnel plus the cognizant scientists associated with the data automation system (DAS), scan subsystem and television (TV) subsystem, and

(3) science data support personnel.

The subgroups are directed by the assistant project scientist, project engineer and science data coordinator, respectively. Each subgroup has been appropriately staffed and individual tasks assigned.

The first subgroup established the facilities required (during encounter) by the personnel working with the

assistant project scientist. It is also studying the probable Martian environment in order to predict the occurrence of planet-induced phenomena. This information will aid the spacecraft performance analysis and command group to predict and analyze the performance of other spacecraft subsystems. To support the analysis of cruise instrument data in near real-time, computer programs have been specified. Most of the programs are in existence and have been utilized throughout the mission for nonreal-time analysis; some are new.

The second subgroup, directed by the project engineer, has similarly established its needs for facilities. One of these is the installation of equipment for direct on-line processing of the real-time telemetry. This equipment bypasses the usual facility computer processing and provides a means for receiving immediate indications of spacecraft events such as planet acquisition by the wide and narrow angle sensors and the TV instrument. Having this information several minutes before it is available on the standard output devices reduces reaction time during this most critcal phase of the mission. This equipment also provides a readily-interpretable display of all other science data and can therefore be used for real-time science analysis in the event of failures in the primary data processing equipment. The equipment has been installed and was used during two preparedness tests with excellent results.

Members of the second subgroup are also responsible for computing times for the transmission of various commands both in the nominal sequence and in nonstandard sequences. To aid in this, several special computer programs are required, such as: time versus DAS frame count and planet scan subsystem data as a function of time. During encounter operations, it will be necessary to run the time versus frame count program as often as necessary to eliminate the possibility for error. During recent tests, it was shown that the program output could be in the user's hands within 10 minutes after the request. Additional recent activities of this subgroup are the generation of nominal expected parameter values of TV and scan subsystem functions. The information was derived from extensive controlled-environment tests of models of these instruments.

The third subgroup, the data handling subgroup, is responsible for seeing that computer programs are written, tested and implemented and that all output data are distributed expeditiously. To this end, procedures have been established outlining the requirements of the users and the proposed methods of meeting these requirements. One program, the special scan program, predicts the motion of the scan platform on the basis of received real-time telemetry as input and it outputs a time to send the inhibit command such that the platform attains the proper clock angle for the TV trace. If the command is not sent, the program output is used in conjunction with another program to predict the intercept point on the planet limb for both a searching and tracking scan subsystem. The program is expected to be ready for test during the next reporting period. In addition to these user programs, simulated data on magnetic tapes have been prepared for use in program checkout and personnel training.

c. Other activities. Tests have been performed on the proof test model (PTM) spacecraft and on available spare instruments involving the DAS, scan subsystem, and TV subsystems to answer specific questions on the encounter sequence. To date, three full scale encounter tests, one in simulated real time covering 26 hr, and two scan positioning tests have been performed in preparation for encounter.

References

1. Rossi, Bruno, *High-Energy Particles,* Prentice-Hall, Inc., New York, 1952.

2. Mathison, Richard P., *Mariner Mars 1964 Telemetry and Command System,* Technical Report No. 32-684, Jet Propulsion Laboratory, Pasadena, June 1, 1965.

3. Bube, R. H., *Photoconductivity of Solids,* Chap. 8, John Wiley and Sons, Inc., New York, 1960.

UNCLASSIFIED

II. *Voyager* Project

A. Introduction

The primary objective of the *Voyager* Program is the performance of unmanned experiments on the surface of, and in orbit about, the planet Mars in order to obtain information concerning the existence and nature of extraterrestrial life, the atmospheric and the surface characteristics of the planet, and the planetary environment. The secondary objective is the acquisition of scientific information concerning the interplanetary media.

All *Voyager* missions will be conducted as events of an integrated program in which each individual flight forms a part of a logical sequence in an over-all technical plan of both lander and orbital operations. The *Voyager* design will provide for the carrying of large scientific payloads to the planet, the telemetering of a high volume of data back to Earth, and long and useful lifetimes in orbit about the planet and/or on the planetary surface. Hardware will be designed to accommodate a variety of spacecraft and/or capsule science payloads, mission profiles, and trajectories. Particular emphasis will be given to simple design, feasible redundancy, and a comprehensive program of component, subsystem, and system testing.

Over-all direction and evaluation of the *Voyager* Program is the responsibility of the Office of Space Science and Applications (OSSA) of the National Aeronautics and Space Administration (NASA). Management of the *Voyager* Project and implementation of selected systems is the responsibility of the Jet Propulsion Laboratory of the California Institute of Technology.

Two *Voyager* space vehicles are to be designed, constructed, and tested for launch during the 1971 Mars opportunity. Attention is also being given to requirements imposed on such vehicles by launches subsequent to 1971, such as missions planned for 1973 and 1975. The over-all flight spacecraft is to consist of a flight spacecraft and a flight capsule. The flight spacecraft, which will have a dry weight of approximately 2,000 lb and will carry several hundred pounds of scientific instruments, will be a fully attitude-stabilized device utilizing celestial references for the cruise phase and will be capable of providing velocity increments for midcourse trajectory correction and for Mars orbit attainment; onboard sequencing and logic will be provided, as will a ground command capability. The spacecraft will supply its own power from solar energy or from internal sources and will be capable of maintaining radio communications with Earth. In addition, the

UNCLASSIFIED

spacecraft will be thermally integrated and stabilized and will monitor various scientific phenomena near Mars and during transit, and telemeter this information back to Earth. It will also monitor and telemeter data pertaining to spacecraft operation. The flight spacecraft will also provide the flight capsule with services such as power, timing and sequencing, telemetry, and command during the transit portion of the missions and may also serve as a communications relay. The flight capsule will be designed for entry into the Mars atmosphere, descent to the surface, impact survival, and surface lifetimes of as much as six months and will contain the power, guidance, control, communications, and data-handling systems necessary to complete its mission.

Appropriate deep-space flight tests of elements of the flight spacecraft are planned approximately two years earlier than the 1971 missions, and preferably in the 1969 Mars opportunity, in order to permit evaluation of *Voyager* components and subsystems during long life in space and to demonstrate operations procedures. The test program for the flight capsule, which includes Earth-entry flight tests, will investigate entry, descent, impact, communications technology, and sterilization. The launch vehicle for the 1971 and immediately subsequent *Voyager* operations will be the *Saturn 1B*, with a *Centaur* as the third stage. The 1969 test flights will use either the *Saturn 1B/Centaur* configuration or an *Atlas/Centaur* combination. The earlier Earth-entry test flights will probably be launched by an *Atlas*.

B. Spacecraft Design

1. Abstract

A concept of spacecraft electronic packaging, representing a logical evolution of *Ranger* and *Mariner* packaging concepts and techniques, is described. Four packaging techniques which could satisfy the majority of *Voyager* requirements are presented.

The methods and processes group reports on soldering techniques to be used when soldering stranded wires into connector solder cups.

Current JPL Mars engineering atmosphere and surface models are discussed, together with the models themselves. Twelve model atmospheres, which permit the various "worst case" entry and terminal descent problems to be investigated, and two surface characteristic models are presented; one for the bright areas, and the other for the dark areas.

Some preliminary investigations of the angle of attack envelope of large aerodynamic entry bodies are discussed. An interesting correlation between the results of the linear theory and a general nonlinear six-degree-of-freedom solution is discussed.

Recently developed weight curves are presented for estimating the aeroshell structural weight of large Martian entry bodies.

2. Spacecraft Packaging and Cabling

a. Packaging design concept. Although the *Voyager* spacecraft configuration is not yet determined, general packaging techniques and configurations are being independently developed. A desirable configuration for complex electronic equipment is one which has many flat, separable surfaces for mounting and interconnecting electronic components. These surfaces, formed in trays and fastened together, can be effective spacecraft structural members. This integrated structural design concept has been used on *Ranger* and *Mariner* with increasing efficiency.

Fig. 1 shows a typical electronic assembly. Here, electronic subassemblies or "trays" are fastened between two structural-thermal plates. The inner plate contains floating connectors and fixed interconnecting cables. This design reduces the hazards of damage through flexing of harnesses, provides for use of shorter wires with direct routing, and protects connector pins through straight mating with use of guide pins. In this figure, the subassemblies are shown of two profiles—half and full size. The subassembly width or thickness is flexible. Thus, once the spacecraft configuration is evolved, standard subassemblies can be readily developed.

b. Packaging techniques. To improve reliability and to provide fabrication control, four well-defined packaging techniques are proposed.

Terminal connected planar packaging technique. This technique is the well-proven two-dimensional flat layout on printed wiring boards. It is proposed to use this technique for power supplies or whenever component sizes are greatly different. Fig. 2 shows the general configuration of the planar packaging technique. Here, different types

of components are shown in their typical mounting method. The process requirements are shown for each application. The planar technique allows maximum design flexibility and easy component replacement capability.

Wire connected cordwood module packaging technique. A higher density three-dimensional technique is utilized while retaining some design and change flexibility. Fig. 3 shows a typical configuration of "wirecon."

This design utilizes welded cordwood modules and interconnects the modules with a soldered wire harness. Each module utilizes a standard header which provides terminals for interconnections and leads for connections to components. The header leads are positioned perpendicular to the component leads to provide greater design flexibility inside the module. Since this configuration does not require preselection of lead positions on the header, module design is further simplified. Such a module can be designed independently of its use by selecting module height and number of terminals in the header as needed. The modules are mounted in the subchassis with a fastener integral with the header. The header terminals protrude through the subchassis and are soldered to the interconnecting harness.

This technique offers high density packaging together with easy module replacement and easy change in interconnections. Although this design concept is new it utilizes well-proven processes. An application of this design is being incorporated in the OGO E plasma probe, and prototype hardware is being fabricated for qualification and testing.

Matrix connected modular packaging technique. This technique utilizes welded cordwood modules and interconnects them with a multilayer interconnecting board. General configuration of this technique is shown in Fig. 4. Welded modules have terminal leads in a preselected pattern which fits the subchassis and interconnecting board hole pattern. Then the module leads are connected by welding to separate ribbons to the risers on the board. The carrier board can be made either with welded ribbon matrix or a multilayer printed wiring board.

This technique offers the advantage of a reproducible interconnecting configuration. The module design is somewhat more difficult, since lead position selection is desirable to minimize the layers of interconnections. This technique requires firm interconnect design, since changes are more difficult to incorporate.

The matrix connected modular and planar packaging techniques have been successfully used on *Ranger* and *Mariner* spacecraft. Refinements are planned to increase reliability.

Integrated circuit modular packaging technique. This technique is shown in Fig. 5. Here, integrated circuits are mounted on one side of a plastic housing while the other side contains magnet wire interconnections. Integrated circuit chips are parallel gap welded to the feed-through terminals. Soldered magnet wire provides simple and flexible interconnections. The arrangement of terminals within the plastic housing is such that module external leads can be mixed in a preselected way to simplify interconnections between the modules and subassembly connectors. With module lead selection, wire crossing can be reduced to a minimum and in many cases entirely eliminated. The use of a common housing provides design standardization, ease of fabrication, and subsequent testing through a common test connector.

This packaging technique is also to be used on the OGO E plasma probe. Prototype housings and terminals have been fabricated and processes have been developed for welding the integrated circuit leads and soldering magnet wire interconnections. Complete evaluation and qualification tests are planned during the following months.

These four packaging techniques are expected to satisfy the requirements of the majority of *Voyager* electronic equipment. Design specifications have been generated to cover the packaging process and material requirements. The present issue of these specifications contain limited thermal and dynamic design information; however, future tests will provide the necessary data.

3. Methods and Processes Developments

Concurrent with the definition of spacecraft packaging and cabling design requirements and the definition of techniques, the associated methods and processes are being developed. Many of these processes have been used on previous flight projects and are being refined and documented. Other processes have had known deficiencies and inadequate process margins and are, therefore, being more carefully evaluated and tested. Furthermore, new processes are required to cover new packaging techniques, particularly in the use of integrated circuits.

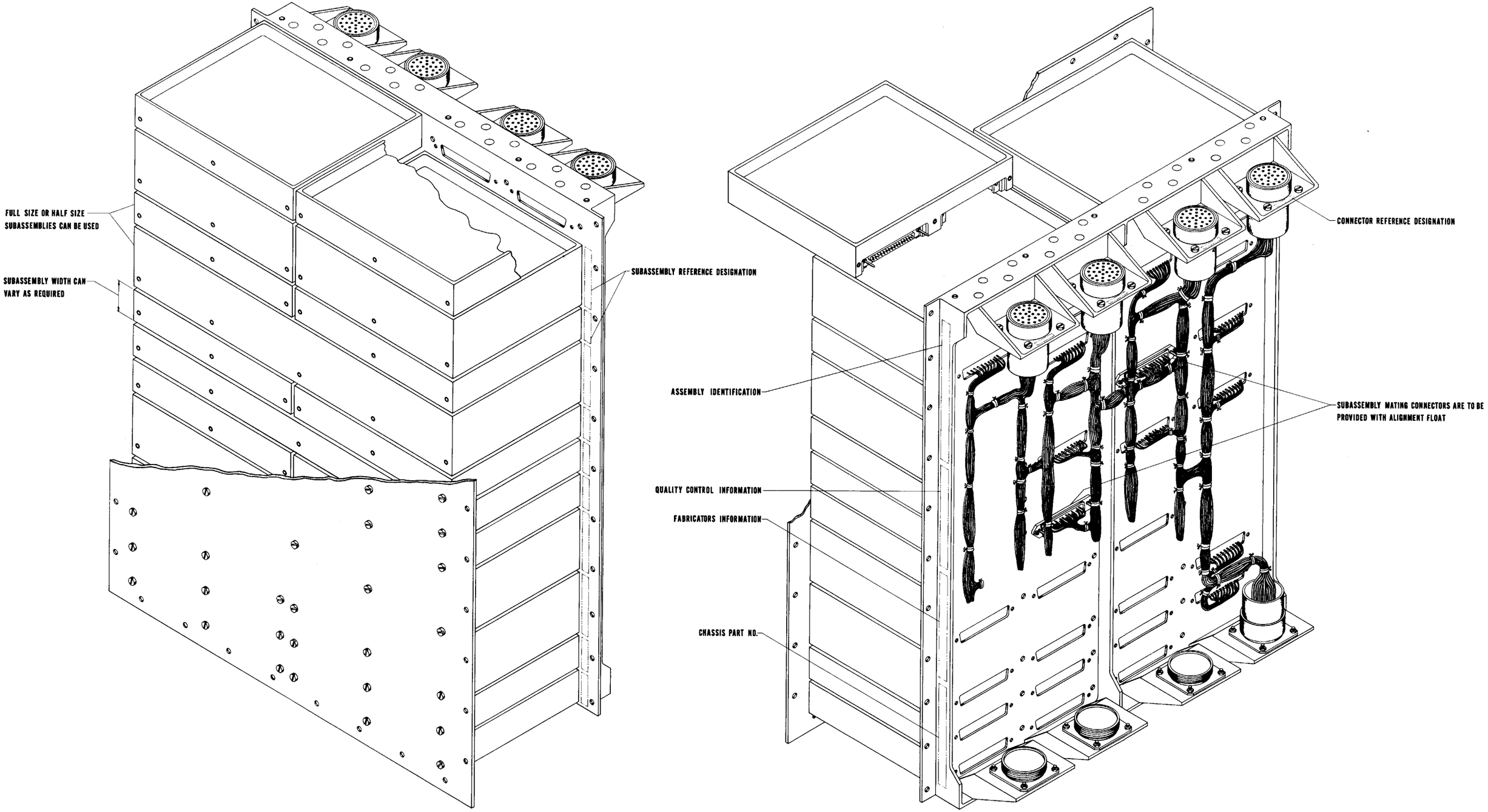
FULL SIZE OR HALF SIZE SUBASSEMBLIES CAN BE USED
SUBASSEMBLY WIDTH CAN VARY AS REQUIRED
SUBASSEMBLY REFERENCE DESIGNATION
CONNECTOR REFERENCE DESIGNATION
ASSEMBLY IDENTIFICATION
SUBASSEMBLY MATING CONNECTORS ARE TO BE PROVIDED WITH ALIGNMENT FLOAT
QUALITY CONTROL INFORMATION
FABRICATORS INFORMATION
CHASSIS PART NO.

Fig. 1. Typical electronic assembly

UNCLASSIFIED

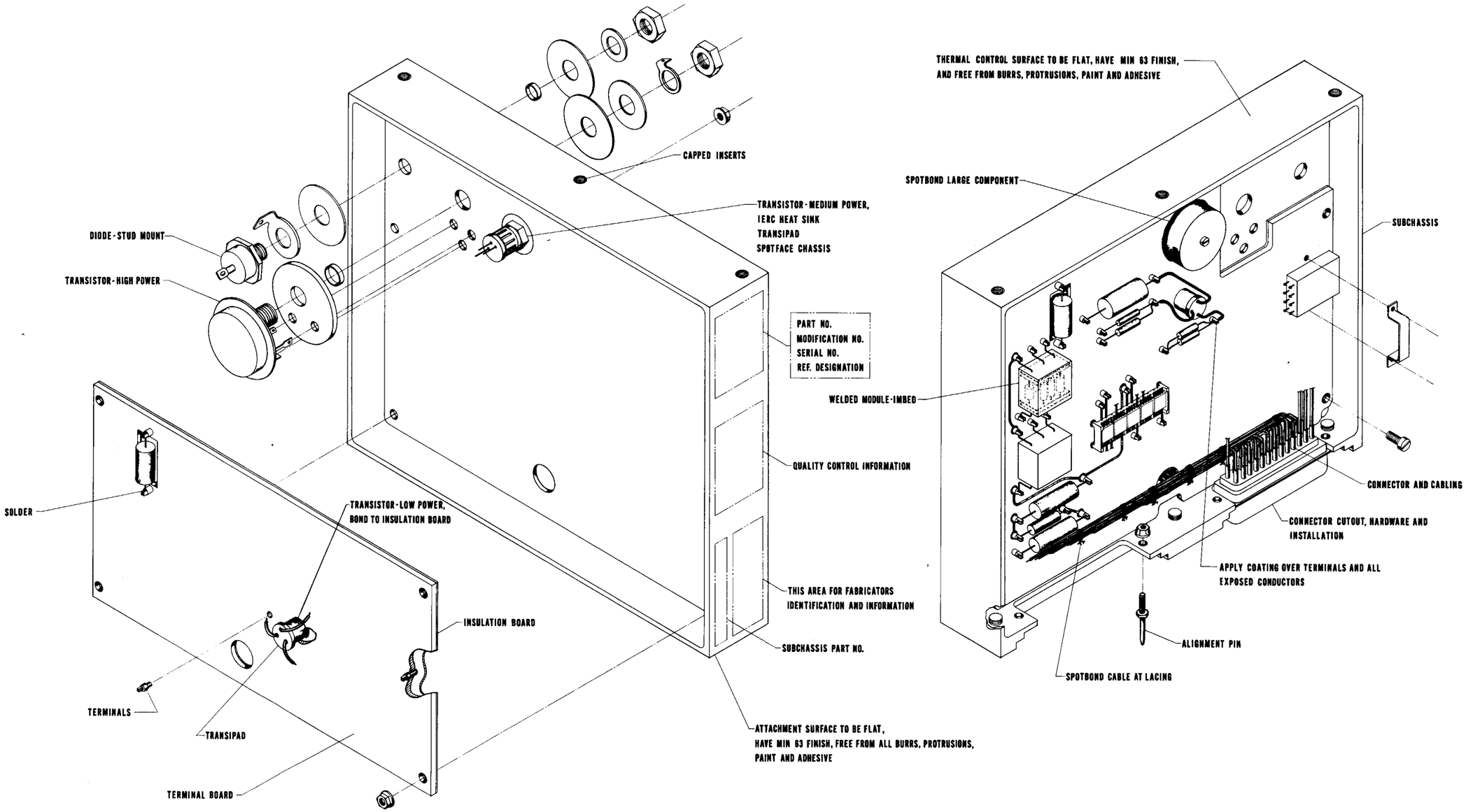

Fig. 2. Planar packaging configuration

UNCLASSIFIED

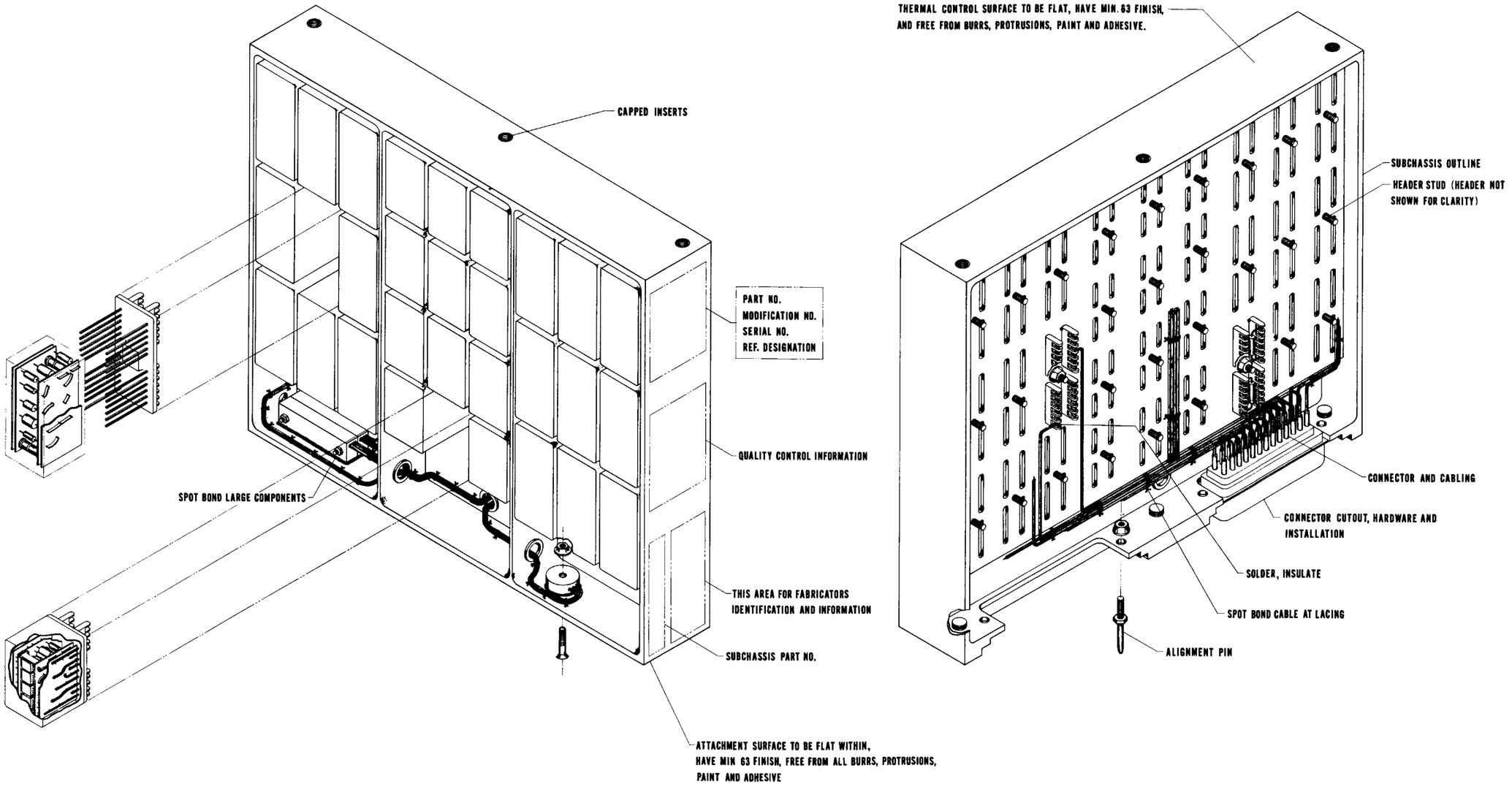
CAPPED INSERTS
PART NO.
MODIFICATION NO.
SERIAL NO.
REF. DESIGNATION
QUALITY CONTROL INFORMATION
SPOT BOND LARGE COMPONENTS
THIS AREA FOR FABRICATORS IDENTIFICATION AND INFORMATION
SUBCHASSIS PART NO.
ATTACHMENT SURFACE TO BE FLAT WITHIN, HAVE MIN 63 FINISH, FREE FROM ALL BURRS, PROTRUSIONS, PAINT AND ADHESIVE
THERMAL CONTROL SURFACE TO BE FLAT, HAVE MIN. 63 FINISH, AND FREE FROM BURRS, PROTRUSIONS, PAINT AND ADHESIVE.
SUBCHASSIS OUTLINE
HEADER STUD (HEADER NOT SHOWN FOR CLARITY)
CONNECTOR AND CABLING
CONNECTOR CUTOUT, HARDWARE AND INSTALLATION
SOLDER, INSULATE
SPOT BOND CABLE AT LACING
ALIGNMENT PIN

Fig. 3. Wire connected modular packaging configuration

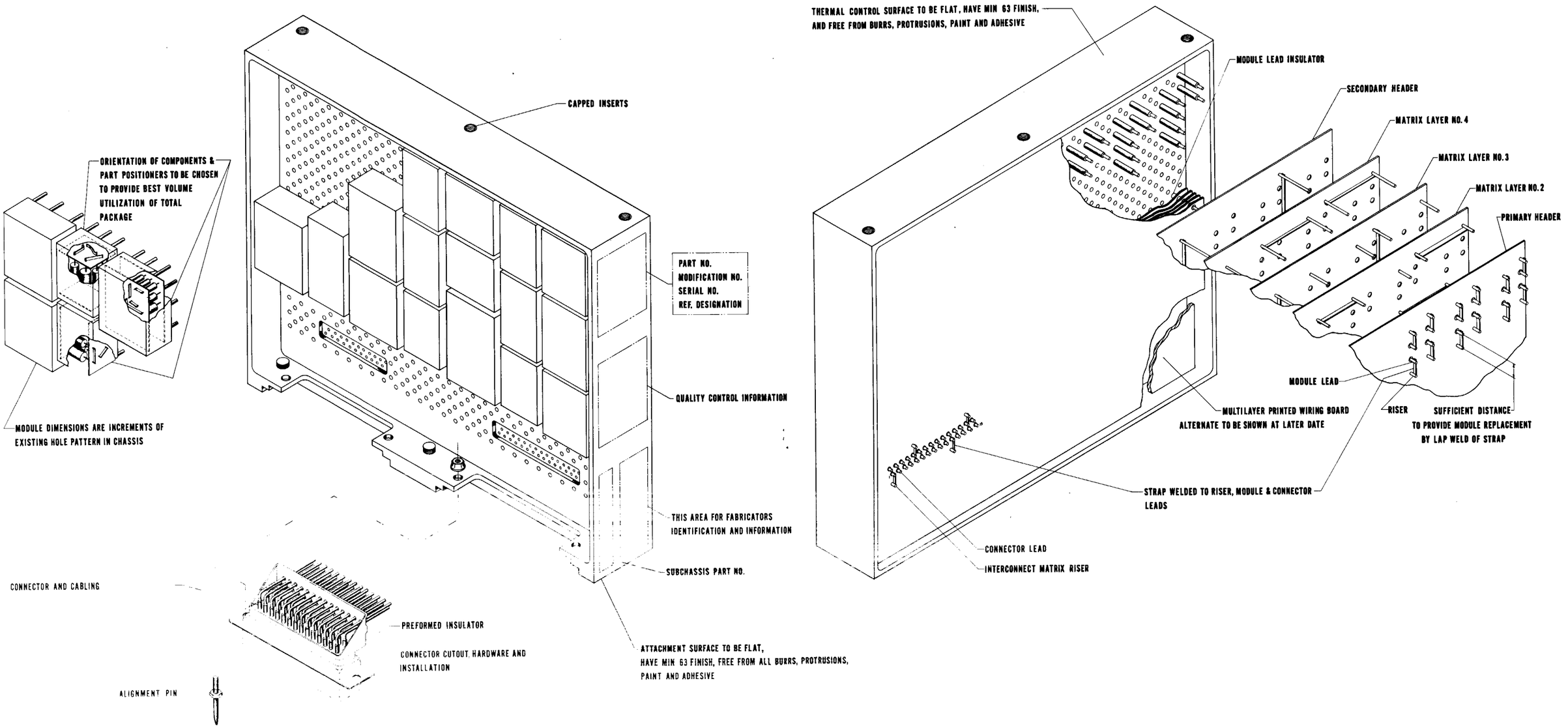
ORIENTATION OF COMPONENTS & PART POSITIONERS TO BE CHOSEN TO PROVIDE BEST VOLUME UTILIZATION OF TOTAL PACKAGE
MODULE DIMENSIONS ARE INCREMENTS OF EXISTING HOLE PATTERN IN CHASSIS
CAPPED INSERTS
PART NO.
MODIFICATION NO.
SERIAL NO.
REF. DESIGNATION
QUALITY CONTROL INFORMATION
THIS AREA FOR FABRICATORS IDENTIFICATION AND INFORMATION
SUBCHASSIS PART NO.
ATTACHMENT SURFACE TO BE FLAT, HAVE MIN 63 FINISH, FREE FROM ALL BURRS, PROTRUSIONS, PAINT AND ADHESIVE
CONNECTOR AND CABLING
PREFORMED INSULATOR
CONNECTOR CUTOUT HARDWARE AND INSTALLATION
ALIGNMENT PIN
THERMAL CONTROL SURFACE TO BE FLAT, HAVE MIN 63 FINISH, AND FREE FROM BURRS, PROTRUSIONS, PAINT AND ADHESIVE
MODULE LEAD INSULATOR
SECONDARY HEADER
MATRIX LAYER NO. 4
MATRIX LAYER NO. 3
MATRIX LAYER NO. 2
PRIMARY HEADER
MODULE LEAD
MULTILAYER PRINTED WIRING BOARD
ALTERNATE TO BE SHOWN AT LATER DATE
RISER
SUFFICIENT DISTANCE TO PROVIDE MODULE REPLACEMENT BY LAP WELD OF STRAP
STRAP WELDED TO RISER, MODULE & CONNECTOR LEADS
CONNECTOR LEAD
INTERCONNECT MATRIX RISER

Fig. 4. Matrix connected modular packaging configuration

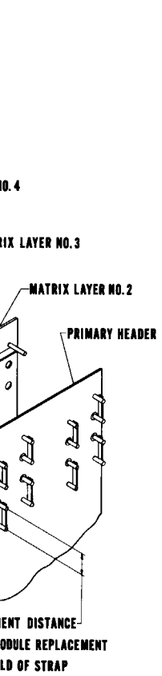

ng configuration

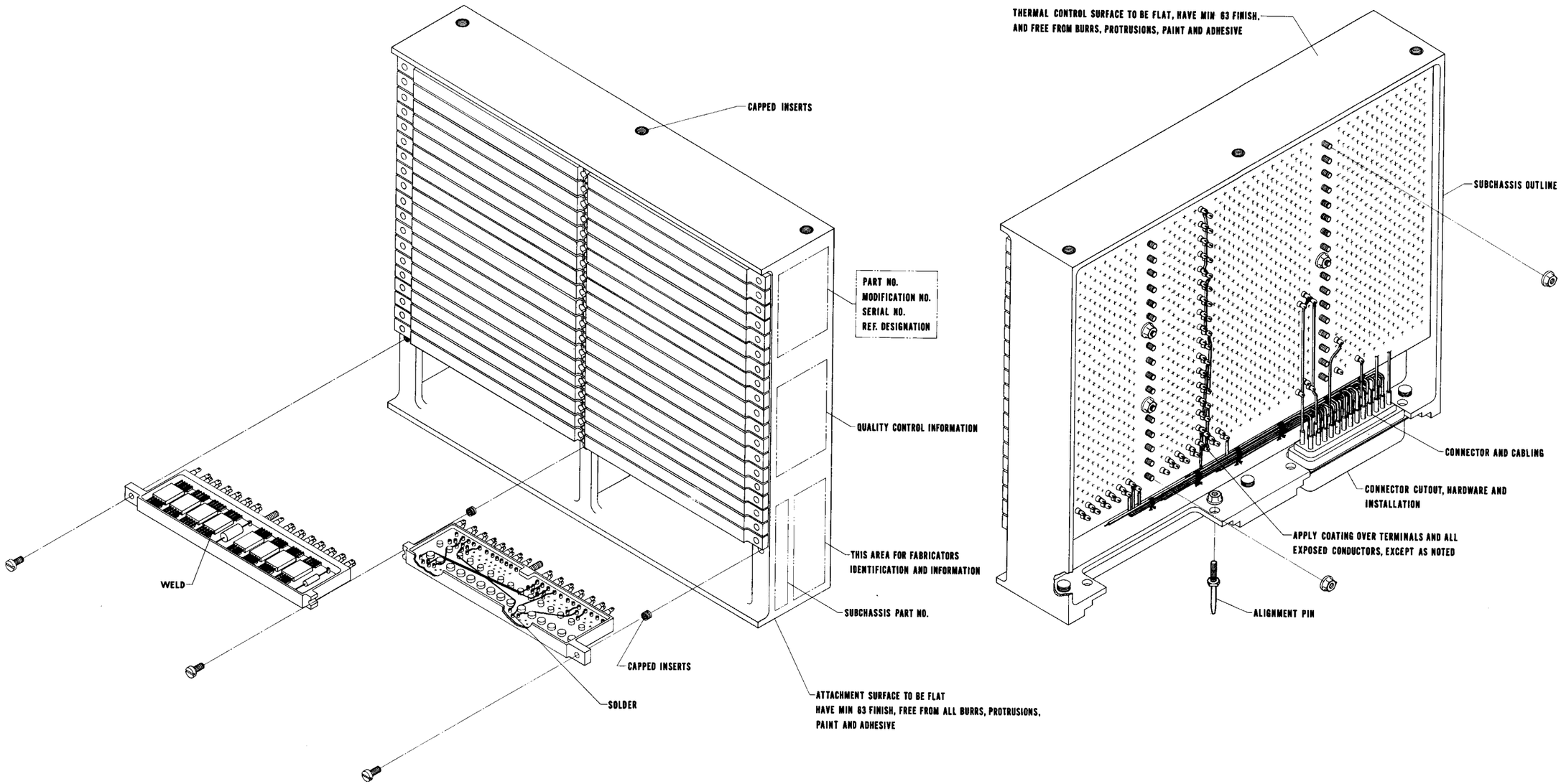
CAPPED INSERTS
PART NO.
MODIFICATION NO.
SERIAL NO.
REF. DESIGNATION
QUALITY CONTROL INFORMATION
THIS AREA FOR FABRICATORS IDENTIFICATION AND INFORMATION
SUBCHASSIS PART NO.
WELD
CAPPED INSERTS
SOLDER
ATTACHMENT SURFACE TO BE FLAT
HAVE MIN 63 FINISH, FREE FROM ALL BURRS, PROTRUSIONS,
PAINT AND ADHESIVE
THERMAL CONTROL SURFACE TO BE FLAT, HAVE MIN 63 FINISH,
AND FREE FROM BURRS, PROTRUSIONS, PAINT AND ADHESIVE
SUBCHASSIS OUTLINE
CONNECTOR AND CABLING
CONNECTOR CUTOUT, HARDWARE AND INSTALLATION
APPLY COATING OVER TERMINALS AND ALL EXPOSED CONDUCTORS, EXCEPT AS NOTED
ALIGNMENT PIN

Fig. 5. Integrated circuit packaging configuration

Results of recent development work and qualification tests are as follows:

a. Protective covering of solder coating during handling and storage. To protect the printed wiring boards and other solder joints during storage and handling, fourteen materials were evaluated for

(1) solvent removal procedures

(2) protection afforded by the coating against corrosion

(3) effect of soldering temperature on the coating

(4) fungus resistance

(5) compatibility with the presently used compound coating

(6) ease of coating application methods

Lonco No. 21-XR was found to be the most effective material and could be readily applied by either dip or brush method.

b. Soldering to connector solder cups. A procedure has been selected for soldering stranded wires into connector solder cups to produce a controlled and reliable solder joint. This work consisted of determining the optimum soldering iron tip shape, size, and temperature together with the method of wire tinning, location of heat application, connector cup orientation, and the method of tinning the connector cup. Work was also done in determining the soldering time required using two different wire gages together with the optimum procedures determined above. The basic conclusions of the task were

(1) the method used to tin stranded wire affects the ultimate strength of the solder joint

(2) the orientation of the solder cup during soldering does not significantly affect the resultant solder joint

(3) the form of the solder preform (solid versus cored) affects the ultimate strength and number of included voids in the solder joint

(4) extended heating degrades the appearance but not the strength of the solder joint

(5) extended heating of the solder joint causes excessive wicking of solder into the strands of the wire, resulting in large voids in the bottom of the cup

(6) solder cup solder joints will include voids regardless of the soldering technique used

4. Mars Engineering Atmospheric and Surface Models

The development of Mars atmospheric and surface models[1] may result in significantly different models depending on whether the model is required for an engineering subsystem or a scientific instrument design. The Mars models contained herein are developed solely for the purpose of estimating critical design conditions for a Mars capsule-lander; however, all the models are internally consistent. Mars atmospheric models which have been developed encompass the "expected" worst conditions for the design of the capsule structure and heat shield, terminal decelerator (typically a parachute) and available descent time in the atmosphere. Separate engineering models of the Mars surface and terrain have been developed for the bright areas and the dark areas in order to get an engineering comparison of the difficulty in landing in either of these areas. The surface model is required in order to properly design the landing energy absorber, evaluate the dynamics of impact, and evaluate the landed payload orientation and other payload support systems.

Observational data of the Mars atmosphere and surface features is extremely limited at this time. The Mars models described are developed from ground-based observational data combined with analytical techniques to obtain nonobservable properties. Many of the physical properties and characteristics of Mars were estimated by considering analogous (hopefully) conditions on the Earth. *Mariner IV* data may provide sufficiently better information to allow a redefinition of some of these models.

The atmospheric properties of prime importance in these models are the Mars surface pressure and atmospheric winds. The basis for the Mars surface pressure design models was the combined spectroscopic data of Kaplan, Munch and Spinrad (Ref. 1) and Kuiper (Ref. 2). The comparative interpretation of these data, as well as other data, is shown in Fig. 6. The recommended engineering atmospheric models (Table 1) has a minimum surface pressure of 14 mb, a mean surface pressure of 25 mb, and a maximum surface pressure of 40 mb. Models are also presented in Table 1 consistent with an absolute lower bound surface pressure of 7 mb, but these are not recommended for design purposes.

Variations in the Mars atmospheric models for a given surface pressure result from various critical atmospheric

[1]The rationale and detailed development is presented in Jet Propulsion Laboratory technical memorandum No. TM 32-234.

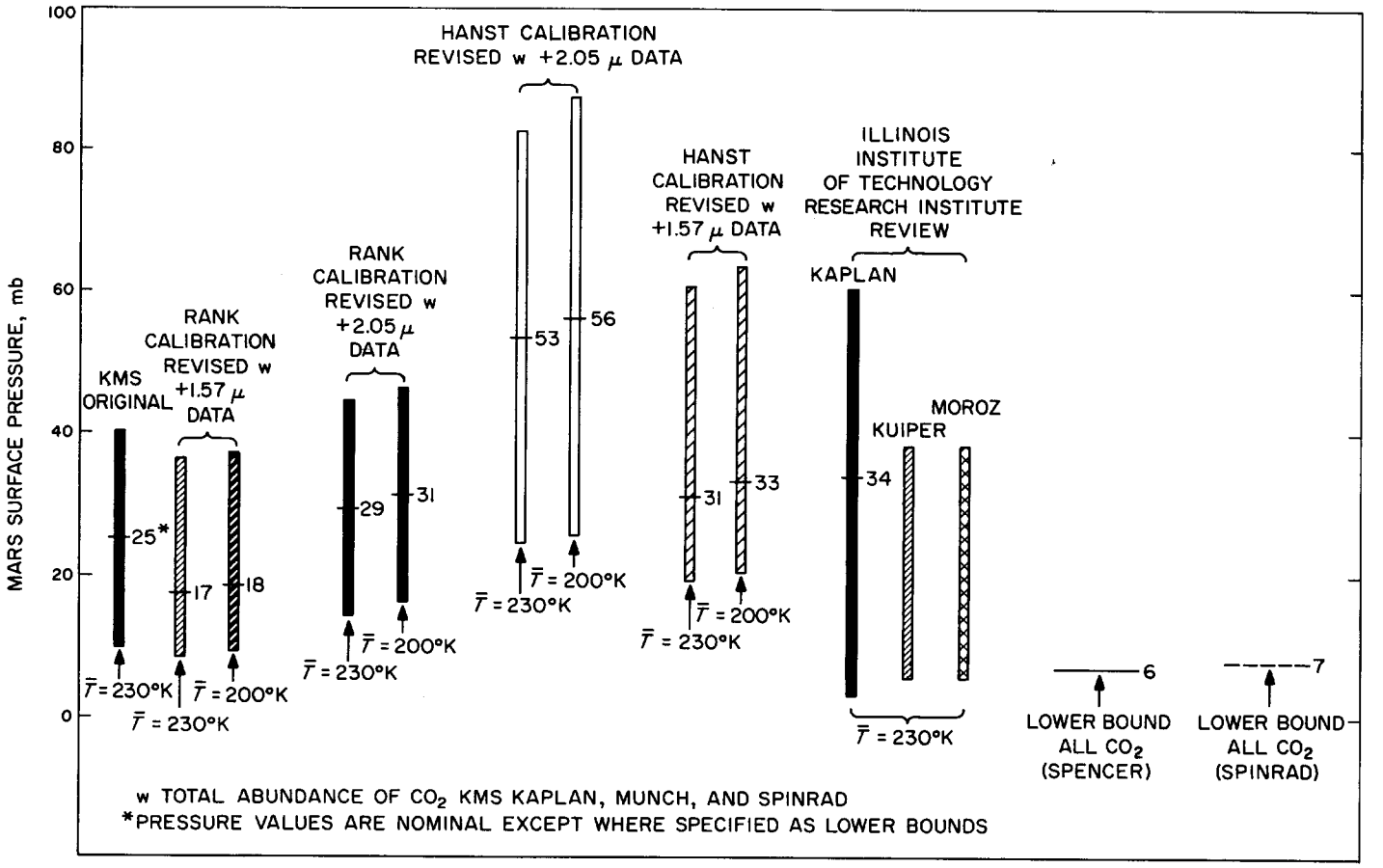

Fig. 6. Summary of Mars surface pressure interpretations. (All interpretations depend upon a single plate by Kaplan, Munch and Spinrad.)

temperature distributions. The critical surface temperature for terminal descent is the model with the lowest surface atmospheric density, i.e., the maximum surface temperature for a given surface pressure. The maximum atmospheric surface temperature is 300°K (models M 69-1, -4, -5, -6, -7, -8, and -9). The critical troposphere temperature distribution for deployment of a terminal decelerator is the model which has the lowest pressure at a given altitude. This model results for a minimum atmospheric surface temperature and minimum stratospheric temperature. The minimum atmospheric surface temperature is 200°K (models M 69-3, -10, -11, and -12).

The stratospheric temperature is the major factor in determining peak entry loads and total heating. The maximum capsule deceleration and total radiative heating occur for the minimum stratospheric temperature (100°K) while maximum total convective heating occurs for the peak stratospheric temperature (260°K).

The other major atmospheric property affecting descent system design is the Mars atmospheric winds. The wind model is based on observed motions of yellow and white clouds in the Mars atmosphere coupled with theoretical calculations regarding the wind velocities necessary to form these clouds. Based on the very limited data, a surface wind speed of approximately 100 ft/sec is recommended for surface pressures from 14 to 40 mb. A mean vertical wind gradient of 2 ft/sec/1000 ft to an altitude of 50,000 ft is also recommended. The terminal decelerator should also be capable of accommodating gust wind speeds of 200 ft/sec. These winds should be considered to be in downslope, upslope, or cross-slope directions depending on which direction is critical. Peak wind speeds are 330 ft/sec (14 mb), 250 ft/sec (25 mb) and 200 ft/sec (40 mb). These values should be used to determine long-term (>1 mo) lander stability requirements.

The atmospheric models presented in Table 1 also present other derived atmospheric properties. The

Table 1. Mars atmospheric models

Property	Symbol	Units	M 69-1[a]	M 69-2	M 69-3	M 69-4	M 69-5	M 69-6	M 69-7	M 69-8	M 69-9	M 69-10	M 69-11	M 69-12
Surface pressure	P_o	mb	25	14	7	7	14	14	25	40	40	14	14	25
		lb/ft^2	52.2	29.2	14.6	14.6	29.2	29.2	52.2	83.5	83.5	29.2	29.2	52.2
Surface density	ρ_o	(gm/cm^3) 10^5	2.92	2.10	1.65	1.10	1.74	1.74	2.92	4.55	4.55	2.62	2.62	4.38
		(slugs/ft^3) 10^5	5.66	4.08	3.20	2.13	3.38	3.38	5.66	8.84	8.84	5.09	5.09	8.49
Surface temperature	T_o	°K	300	250	200	300	300	300	300	300	300	200	200	200
		°R	540	450	360	540	540	540	540	540	540	360	360	360
Stratospheric temperature	T_s	°K	260	180	100	100	100	260	100	260	100	100	200	100
		°R	468	324	180	180	180	468	180	468	180	180	360	180
Acceleration of gravity at surface	g	cm/sec^2	375	375	375	375	375	375	375	375	375	375	375	375
		ft/sec^2	12.3	12.3	12.3	12.3	12.3	12.3	12.3	12.3	12.3	12.3	12.3	12.3
Composition		%												
CO_2 (by mass)			10.6	28.2	78.5	78.5	28.2	28.2	10.6	4.1	4.1	28.2	28.2	10.6
CO_2 (by volume)			7	20	70	70	20	20	7	2.6	2.6	20	20	7
N_2 (by mass)			89.4	71.8	21.5	21.5	71.8	71.8	89.4	95.9	95.9	71.8	71.8	89.4
N_2 (by volume)			93	80	30	30	80	80	93	97.4	97.4	80	80	93
Molecular weight	M	mole^{-1}	29.1	31.2	39.2	39.2	31.2	31.2	29.1	28.4	28.4	31.2	31.2	29.1
Specific heat of mixture	c_p	cal/gm-°K	0.243	0.229	0.183	0.191	0.228	0.234	0.241	0.246	0.245	0.225	0.228	0.240
Specific heat ratio	γ		1.39	1.38	1.38	1.36	1.39	1.37	1.40	1.40	1.40	1.39	1.39	1.40
Adiabatic lapse rate	Γ	°K/km	−3.68	−3.89	−4.88	−4.68	−3.93	−3.83	−3.71	−3.64	−3.65	−3.98	0	−3.73
		°R/1000 ft	−2.02	−2.13	−2.68	−2.57	−2.16	−2.10	−2.04	−2.00	−2.00	−2.18	0	−2.05
Tropopause altitude	h_t	km	10.8	18.0	20.5	42.7	50.9	10.4	53.9	11.0	54.8	25.1	0	26.8
		Kilo-ft	35.6	59.2	67.2	140	167	34.1	177	36.1	180	82.4	0	87.8
Inverse scale height (stratosphere)	β	km^{-1}	0.0505	0.0781	0.176	0.176	0.140	0.0541	0.131	0.0492	0.128	0.140	0.070	0.131
		ft^{-1} × 10^5	1.54	2.38	5.38	5.38	4.26	1.65	4.00	1.50	3.90	4.26	2.13	4.00
Continuous surface wind speed	$\bar{v}_w$	ft/sec	87	116	164	164	116	116	87	82	62	116	116	87
Peak surface wind speed	$v_w^{maximum}$	ft/sec	250	330	470	470	330	330	250	200	200	330	330	250
Design vertical wind gradient	$\frac{d\bar{v}_w}{dh}$	ft/sec/1000 ft	2	2	2	2	2	2	2	2	2	2	2	2

[a]Designation M 69-1 refers to *Mariner* 1969 Mars models. The designation is extended to present *Voyager* efforts.

UNCLASSIFIED
UNCLASSIFIED

atmospheric composition and molecular weight are consistent with the partial pressure of CO_2 used in the total pressure estimate and the assumption that the remaining constituent is nitrogen.

Engineering surface and terrain models are developed for the bright areas and dark areas of Mars. Surface characteristics considered were: general features, composition, relief, slopes, low scale surface contour, roughness, bearing capacity, temperature, density, porosity, specific heat, thermal conductivity, albedo, and emissivity. Table 2 summarizes these characteristics and recommended design requirements. The most significant differences in the design requirements for the bright and dark areas are

(1) the convex and concave low scale surface contour in the dark areas

(2) the 10 cm rock design requirement in the dark areas

(3) the larger range in surface bearing capacity in the dark areas.

In general, it will be much more difficult to design for the full range of Mars surface characteristics in the dark areas than for only the bright areas for the models presented.

Table 2. Summary of Mars surface characteristics and properties

Feature	Bright area	Dark area	Suggested study criteria
Fractional area of Mars surface	0.75	0.25	Both regions
Composition	Limonite to silicates with high contents of Fe_2O_3	Silaceous rocks with 40 to 70% silica, 1 to 18% alumina, 46 to 1% magnesia	Full range of surface compositions
Relief	Low elevation sand dunes	General low elevation with locally high (greater than 10,000 ft) peaks	Zero elevation
Slopes, deg	0 to 45	0 to 30; local slopes of 90	0 to 30
Low scale surface contour	Effectively infinite radius of curvature	Convex and concave surfaces with radii of curvature between 10 cm and ∞	Convex and concave surfaces with radii of curvature between 10 cm and ∞. No landing on peak or hole with a radius curvature between ½ and 2 times the radius of the landed payload
Surface roughness	5 μ to 2 mm diameter sand particles	Coarse (100 μ diameter) sand to 10 cm diameter rocks	Both surface roughnesses
Surface bearing capacity, psi	0.43 to 1.05 B^a	1 to ∞	Both regions
Surface temperature, °K	310 maximum 195 minimum	322 maximum 190 minimum	Both regions
Surface density, gm/cc	1.3 to 1.6	1.2 to 2.6	Both regions
Porosity	0.4 to 0.5	0.5 to 1.0	Both regions
Specific heat, cal/gm °C	0.15 to 0.50	0.15 to 0.30	Both regions
Thermal conductivity, cal/cm sec °C	2×10^{-4} to 4×10^{-3}	5×10^{-4} to 5×10^{-2}	Both regions
Average surface albedo for sunlight	0.15 to 0.35	0.05 to 0.25	Both regions
Average surface emissivity	0.85 to 1.0	0.95 to 1.00	Both regions

[a] B is the breadth of footing in ft.

5. Stability Studies of Large Entry Capsules

Very large entry capsule sizes for Martian entry poses a number of questions. One of these relates to the ability of a large body, entering the atmosphere at high angle of attack, to attain sufficiently low angle of attack at peak heating and dynamic pressure conditions. Since it is often necessary to estimate quickly the aerodynamic performance of different sized bodies (in this instance larger ones) of the same shape, a check was made on the validity of utilizing simplified theories.

From linearized theory and other assumptions on the dynamics of entry, Ref. 3 gives[2]

$$\frac{\alpha_{EN}}{\alpha_E} \propto \left[\frac{\left(\frac{m}{C_D A}\right) I}{C_{m_\alpha} d m}\right]^{1/4} e^{K/[4(m/C_D A)]} \qquad (1)$$

for the angle of attack envelope of a given statically stable shape having a damping coefficient of zero and occurring at a particular ambient density. The ballistic parameter $m/C_D A$ can be assumed independent of size because it is essentially determined by velocity-altitude requirements of a mission. If C_{m_α} is also assumed invariant with size, I/m must vary as d in order to maintain the same angle of attack envelope. Estimates for an assumed *Apollo*-type configuration indicated that I/m varied approximately as d^2, the same as for a solid body. Thus from Eq. 1, α/α_E should vary about as $d^{1/4}$, for a fixed shape, $m/C_D A$, and C_{m_α}.

[2]Nomenclature at end of article.

Since the above simplified approach indicates an increasing angle-of-attack envelope with size, a limited number of 6-degree-of-freedom (DOF) computer runs were made to include the nonlinear case of nearly backward entry and a measured finite damping coefficient. The results are shown in Table 3 as an angle-of-attack envelope at peak convective heating rate and peak dynamic pressure. The 6 DOF computer results are compared with the linear theory predictions, assuming that the 13-ft diameter information was being scaled to a 19-ft case. (For these cases Ip/m varies as $d^{2.16}$ and $d^{2.30}$ for the nominal ballistic coefficients m/C_DA of 0.170 and 0.350, respectively.) It is seen that the predictions are generally within 1 deg of the 6 DOF results for the limited cases considered. It is also possible to obtain similarly good agreement on oscillation frequency. Although using linear theory for scaling purposes appears good, in other cases (e.g., a larger diameter range) the assumption of a zero damping coefficient could be significant. A less approximate version of Eq. 1 would include the product of the damping coefficient and dm/I in the exponent term. Scaling would then require that C_{L_α}/C_D also be known.

Table 3. Effect of entry capsule size on oscillation angle-of-attack envelope[a]

$\frac{m}{C_DA}$ $\frac{\text{slugs}}{\text{ft}^2}$	d, ft	I, slug-ft²	m slugs	$-\gamma_E$ at 800 kft, deg	α_{EN}, deg			
					at Q_{peak}		at q_{peak}	
					6 DOF	Linear theory	6 DOF	Linear theory
0.170	13	520	31.7	90	38	—	34	—
0.170	13	520	31.7	20	26	—	23	—
0.170	19	2500	67.4	90	42	42	37	38
0.170	19	2500	67.4	20	30	29	26	26
0.350	13	675	65.3	90	34	—	28	—
0.350	13	675	65.3	20	23	—	20	—
0.350	19	3430	13.9	90	40	38	33	32
0.350	19	3430	13.9	20	26	26	22	23

[a] $\alpha_E = 170$ deg, $V_E = 25{,}000$ ft/sec, zero pitch and spin rates at entry.

Nomenclature

A maximum cross sectional area of body, ft²

C_D drag cofficient, dimensionless

C_{L_α} lift curve slope

C_{m_α} slope of pitching moment curve

d maximum diameter of body, ft

I pitch or yaw moment of inertia, slug-ft²

K a constant for a given body shape, atmospheric model, entry angle, and zero damping coefficient

m mass of entry body, slugs

Q_{peak} peak stagnation point convective heating rate

q_{peak} peak dynamic pressure

V_E entry velocity, ft/sec

α_E entry angle-of-attack, deg

α_{EN} envelope of angle-of-attack during entry, deg

γ_E entry angle relative to local horizontal, deg

6. Large Capsule Aeroshell Weight Estimates

Structural weight is a large percentage of the total weight of a Mars entry body because a very low ballistic coefficient is required for entry into the minimum surface pressure Mars atmosphere. The *Apollo*-type entry capsule shell has been analyzed to determine, parametrically, the structural weight in terms of several variables. Fiberglass sandwich construction was assumed. The analysis was made for the axisymmetric loading case, although asymmetric buckling was taken into account. Several aluminum sandwich shells were analyzed to compare their structural weights to those calculated in the parametric study. In the lower range of effective loadings, which have been found to be applicable to studies involving low ballistic coefficient bodies, the weight differences were small.

The results of the analysis are expressed, not as structural weights, but as residual weights as a function of capsule diameter, maximum deceleration (at zero angle of attack), aft cone superimposed unit weight, and a parameter called L_e. L_e is a quantity defined as total capsule weight less the forebody superimposed weight, all divided by the projected area of the capsule. This residual weight W_R is the weight of the capsule at entry less the continuous shell structure weight and the total heat shield weight. Therefore, it must include the joints, brackets, fittings, support structure, terminal decelerator, etc., as well as the payload itself.

The data generated in the study[3] are illustrated by the curves in Figs. 7 and 8, which are reproduced from the parametric study. The band shown on the curves of Fig. 8 represents a ±15% uncertainty in the weights, and the lower bounds should be used for design. This uncertainty was assumed, because the structure which is required to

[3] The detailed development and complete study results will be published in the Jet Propulsion Laboratory Technical Memorandum No. 32-236.

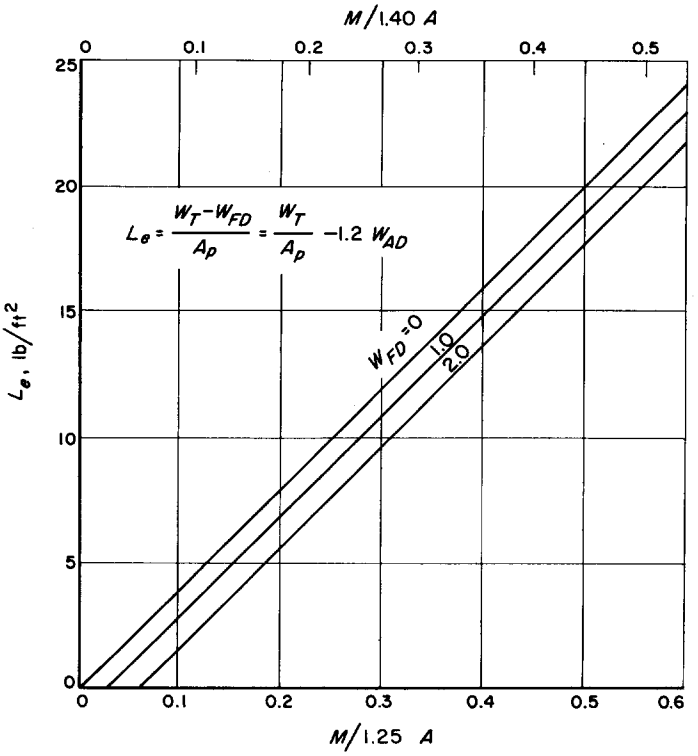

Fig. 7. Conversion chart

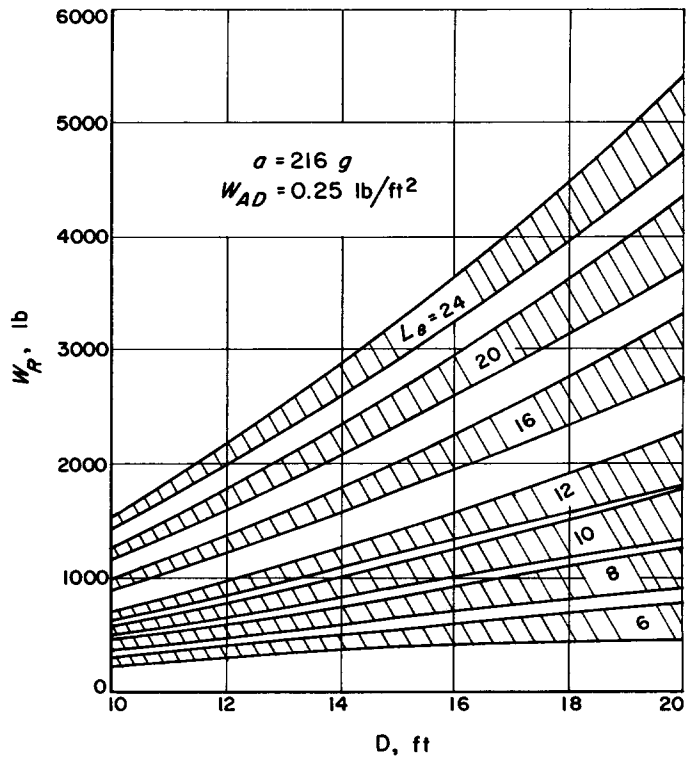

Fig. 8. Residual weight

meet these weights represents an extension of current fabrication practices.

Nomenclature

W_R	residual weight
W_T	total capsule weight at maximum deceleration
M	mass of capsule $W_T/32.2$
W_{FD}	uniformly distributed weight on forebody
W_{AD}	uniformly distributed weight on aftbody
W_{FS}	structural weight of forebody shell
W_{AS}	structural weight of aftbody shell
A_p	projected area of the capsule
L_e	effective loading
D	maximum capsule diameter
a	maximum deceleration (zero angle of attack)

Example:

Given $m/1.25A_p = 0.2$, $D = 15$ in., $W_{AD} = 0.25$ lb/ft², $a = 216\,g$, $W_{FD} = 1.0$ lb/ft²; weight of heat shield material ablated by time of maximum loading = 100 lb

Find W_R, W_T, and W_e

$L_e = 0.2 \times 32.2 \times 1.25 - 1.2\,(1.0) = 6.85$ lb/ft² (or from Fig. 7)

Using linear interpolations between curves for $L_e = 6$ and $L_e = 8$ on Fig. 8

$W_{R\,minimum} = 506$ lb

$$W_T = (L_e + 1.2W_{AD})\,A_p$$
$$= (6.85 + 1.2 \times 1.0)\,\pi/4 \times 15^2$$
$$= 2530 \text{ lb}$$

$$W_e = W_T + 100 \text{ lb} = 2630 \text{ lb}$$

C. Guidance and Control

1. Gas Bearing Gyro Evaluation

a. Abstract. This is a preliminary article on a gas bearing gyro presently under evaluation. The evaluation was conducted by support from the *Voyager* and SR/AD programs. The gyro configuration, test station, and preliminary results are discussed.

b. Gyro configuration. The gyro is a high performance Honeywell model GG159C which has been developed to survive 200 *G*'s shock and 25 *G*'s vibration. Other areas developed for the GG159C, but not incorporated in the particular gyro evaluated, are sterilization, high torquer scale factor, and high frequency gimbal suspension pump. Some of the principle gyro features are as follows:

(1) Single axis rate integrating gyro

(2) Floated gimbal with hydrostatic centering system

(3) Hydrodynamic gas bearing spin motor

(4) Ceramic motor and gimbal construction

(5) Approximately 3 in. long, 2 in. in diameter, and weight of 1 lb

c. Evaluation plan. The evaluation program is designed to determine particular characteristics considered important for a strapdown space application. Tests of special interest are discussed below.

Heading test. The heading test is used to determine torquer scale factor.

Polar tumble test. The polar tumble test is used to determine the drift coefficients: *G* insensitive, *G* sensitive, G^2 sensitive, and random drift rate.

Temperature sensitivity. Because of power limitations for precision temperature control on a spacecraft, it is desirable to utilize a gyro with minimum temperature sensitivity and eliminate active temperature control. For this reason the drift coefficients were determined as a function of temperature from 60 to 130°F.

Suspension System Stiffness. The gyro under test has a stiffer gimbal suspension system than probably is required for a spacecraft attitude control application. Therefore, it is desirable to evaluate the gyro with a reduced suspension system stiffness, because this reduces the fluid error torque. The suspension system stiffness is controlled by varying the hydrostatic fluid pump operating frequency and thereby reducing the fluid flow. The gimbal suspension system, with the pump operating at 20 cps, is sufficiently stiff to maintain gimbal support for input rates to 100,000 deg/hr, according to the manufacturer. Because the gimbal stiffness varies directly as the pump frequency, 25,000 deg/hr turning rates can be tolerated at the lower test frequency of 5 cps. The gimbal suspension system is also satisfactory to support the gimbal in a 1-*G* field for the temperature range and pump frequencies of this test program.

Frequency response. A broad bandwidth is important for autopilot and commanded turn applications. Oscillating rate table tests are planned to evaluate the gyro response.

High G Shock and Vibration. The gyro will be subjected to 200 *G*'s shock and to the *Mariner* Mars 1964 type approval vibration requirements.

d. Test station.

Gyro loop block diagram (Fig. 9).

Heading test. The gyro is mounted with its output axis vertical on a dividing head whose spindle axis is also vertical. The torquer scale factor is calculated from the torquer current measured with the input axis north and south and a knowledge of the horizontal Earth rate component.

Tumble test. The gyro is mounted with its output axis parallel to the tumble table axis, which is parallel to the Earth's axis. The table is driven at a constant rate of 1 revolution/hour and the torquer current is recorded at 10-deg intervals for a total of 36 data points. The current is read with an integrating digital voltmeter using a 10-sec integration period and recorded on paper tape.

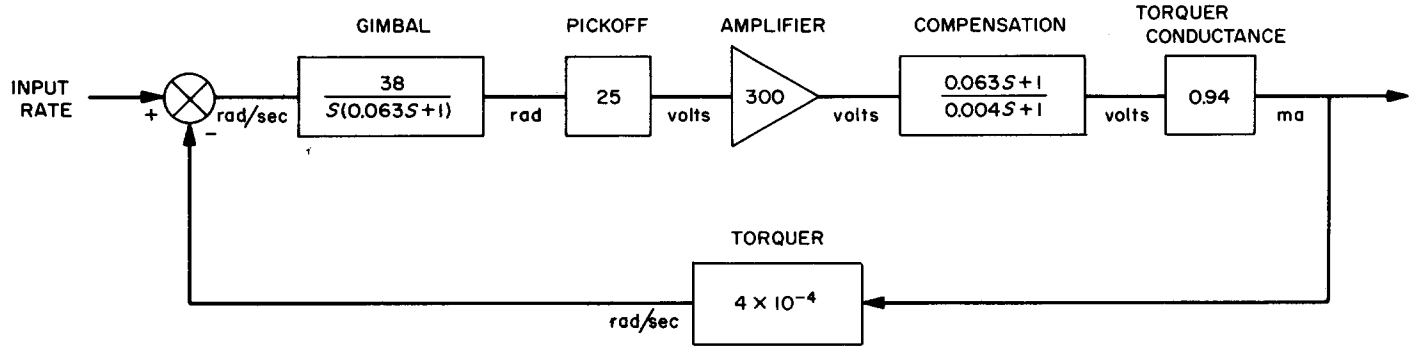

Fig. 9. Gyro loop block diagram

Except for the torquer scale factor all performance data were collected in this manner using two clockwise and two counterclockwise tumble tests for each operating temperature and each pump frequency.

Tumble Test Data Reduction Method. The data are reduced on a computer using a Fourier analysis to extract the bias (G insensitive), first harmonic (G sensitive), second harmonic (G^2 sensitive). Random drift rate is the residual from this analysis. All the data are plotted in the figures.

e. Evaluation results.

G insensitive drift. Fig. 10 shows the G insensitive drift rate. At reduced pump frequency the drift rate change with temperature variation is reduced, indicating the desirability of operating with a low gimbal suspension system stiffness. One may speculate that for this particular gyro there may be a pump frequency (about 2-½ cps) at which the temperature sensitivity of various torque sources (flex leads, fluid flow, signal generator) is such as to result in a very small net drift rate. However, not enough data are available to select the proper curve shapes and accurately predict the drift rate below a pump frequency of 5 cps.

G sensitive drift. Figs. 11 and 12 show MUI (mass unbalance, input axis) and MUS (mass unbalance, spin axis) respectively. MUI is relatively constant with frequency compared to MUS; however, both coefficients show a significant pump frequency sensitivity. The temperature sensitivity is quite large in both cases, indicating the desirability of utilizing the gyro with the output axis vertical for a lander application that may be without good temperature control.

G^2 sensitive drift. Fig. 13 shows the anisoelasticity coefficient. Again we see sensitivity to temperature resulting from bearing clearances varying anisotropically and creating an anisoelasticity change. Sensitivity to pump frequency probably results from gimbal support system anisoelasticity changes. It is worth noting that the stiffest

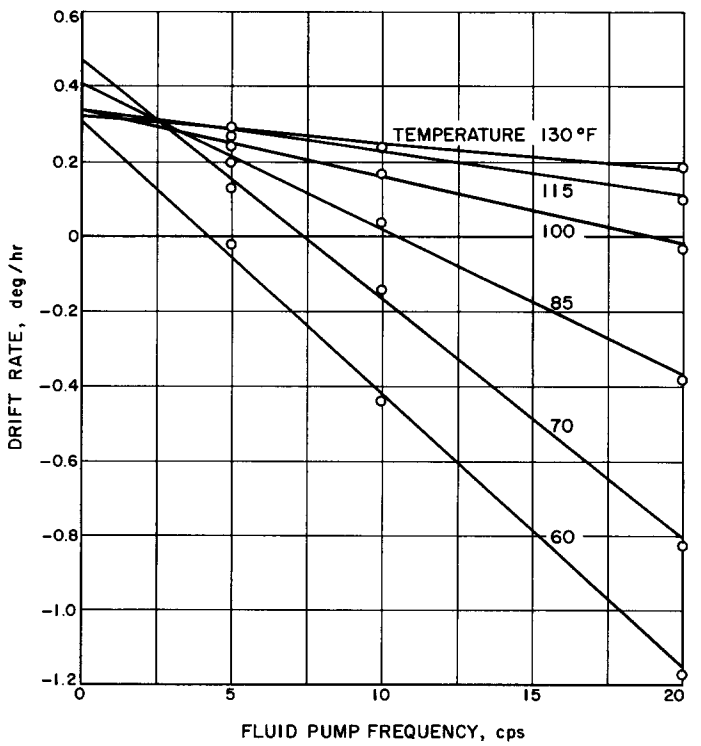

Fig. 10. G insensitive drift rate, G^0

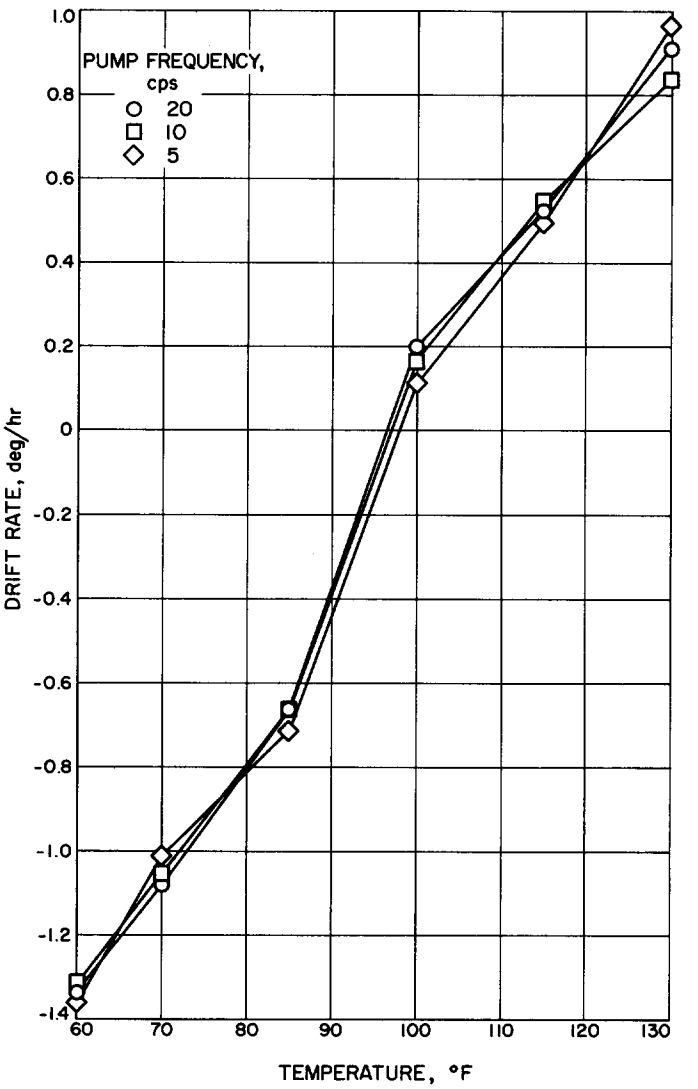

Fig. 11. G sensitive torque, G^1—MUI

suspension system is least sensitive to temperature changes. Because of the gyro attitude during testing there is a contribution from the spin motor attitude angle drift to the anisoelastic coefficient. This contribution will be evaluated in subsequent tumble testing about the input axis horizontal.

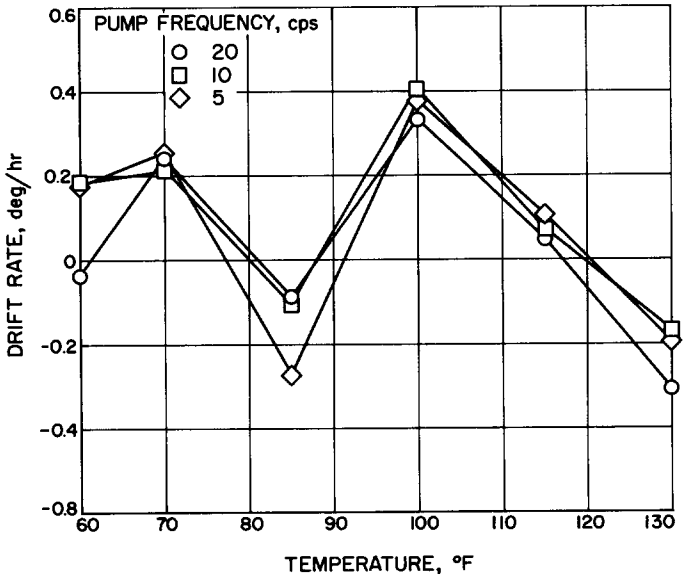

Fig. 12. G sensitive torque, G^1—MUS

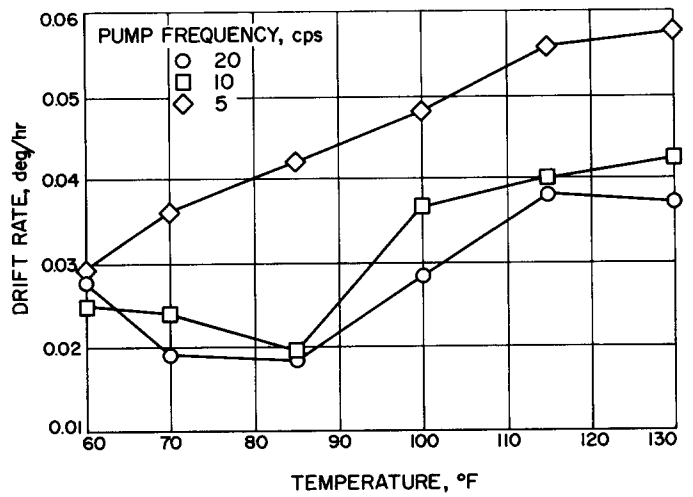

Fig. 13. Anisoelasticity, G^2

Random drift. Fig. 14 shows the random drift rate. The general trend is toward increased random drift with higher temperatures. This is not surprising since the noise level increases with increased temperature. The relatively large sensitivity to frequency at 60°F compared to that at 115 and 130°F may result from a poor pump response at low temperatures. One would suspect that at the higher temperatures the random drift would be most sensitive to suspension system stiffness.

Torquer scale factor. Fig. 15 shows the torquer scale factor as a function of temperature. This calibration allowed use of the proper scale factor for each temperature. The calibration will also be used to check time stability by comparing it with future data.

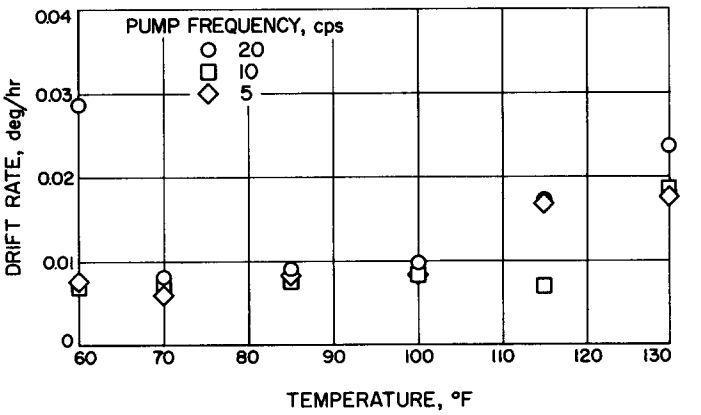

Fig. 14. Random drift

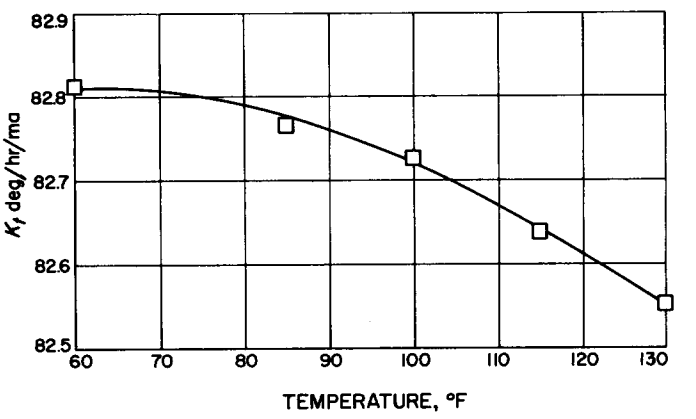

Fig. 15. Torquer scale factor

References

1. Kaplan, L. D., Munch, G., and Spinrad, H., "An Analysis of the Spectrum of Mars," *Astrophysical Journal,* Vol. 139, No. 1, January 1964.
2. Kuiper, G. P., *Communications of the Lunar and Planetary Laboratory,* Vol. 2, No. 31, July 4, 1964.
3. Allen, H. J., *Motion of a Ballistic Missile Angularly Misaligned with the Flight Path Upon Entering the Atmosphere and its Effect Upon Aerodynamic Heating, Aerodynamic Loads, and Miss Distance,* National Advisory Committee for Aeronautics, TN 4048, October 1957.

III. Future Projects

System studies by JPL and industry contractors have determined the gross feasibility and capability of *Voyager*-class Mars landing capsules. Since these studies were completed, a JPL team has been examining specific problems that require attention and advanced development support prior to initiating formal capsule design and procurement processes.

Table 1 lists the objectives of the current six special studies which are scheduled for completion in August 1965.

The lander power study is nearly complete. Preliminary conclusions are as follows:

(1) Solar cells, primary and secondary batteries, monopropellant fueled turboalternators, and radioisotope systems are the most promising for utilization on the *Voyager* capsule. The selection of any one or a combination of these systems is dependent on the mission requirements.

(2) No system is available which will meet all the requirements of a capsule system.

(3) In order to provide a system or systems for capsule and landed operation, intensive development on all the above systems should be started immediately to make them state-of-the-art by January 1967.

Table 1. Special studies of the *Voyager*-class Mars landing capsule

Study	Objective
Capsule and bus deflection:	
(1) Bus deflection	Extension of the mission profile, abort system mechanization, and probability of impact analysis beyond that considered in earlier studies
(2) Capsule deflection	A wide range of attitude and thrust vector control options from the points of view of accuracy, reliability, sterilizability, weight, and power requirements
(3) Comparison	Comparison within and among alternate deflection modes
Relay and direct communications	
(1) Descent relay-link	Analysis of the acquisition problem, telemetry modulation and detection schemes, transmitter and receiver requirements, and capsule and bus antenna requirements
(2) Postlanding direct link	(a) Low bit-rate FSK system (b) Direct link high gain steerable antenna considerations
(3) Postlanding direct and relay (via orbiter) communication links	A systems analysis comparison for an eventual *Voyager* long-life Mars surface mission

UNCLASSIFIED [redacted]

Table 1. Special studies of the *Voyager*-class Mars landing capsule (Cont'd)

Study	Objective
Capsule shape	
(1) Dynamics of entry	Comparison of three shape families (*Apollo*-type, sphere-cone, and smooth-flare) on the basis of velocity-at-altitude and angle-of-attack envelope for a fixed vehicle diameter
(2) Aft-body configuration	Examination of aft-body shape requirements for achieving directional stability at various entry angles-of-attack and consideration of the relationship of aft-body shapes to auxiliary decelerator ejection
(3) Auxiliary decelerators for terminal descent	Preliminary assessment of the aerodynamic performance of an expandable skirt
(4) Low altitude gusts	Assessment of the effect of low altitude wind gusts on the capsule dynamics near impact
(5) Structural deformations	Assessment of the effects on aerodynamic characteristics
(6) Heat shield and structural weights for sphere-cone shape family	A parametric study of the variation of these weight components with nose radius and cone angle, using the JPL (AVCO) computer program
Descent and landing operations	(1) Extension of the earlier ballistic mode study to consider effect of employing large capsule diameters (16 to 19 ft) (2) Determination of whether the capability exists in a large diameter ballistic capsule to carry a parachute engineering experiment (3) Consideration of various terminal deceleration subsystems for tradeoff of increased lander performance with increased operational complexity (4) Examination of *Voyager*-size Mars entry capsule from an aerodynamic stability standpoint (5) Determination of the extents and requirements of the lander from an operations standpoint (orientation, erection, deployment requirements, etc.) Under current re-examination are: (1) Critical temperature profile for ballistic and decelerator modes (2) Mean surface winds, vertical wind gradients, and gust wind conditions (3) Development of Mars surface terrain model
Lander power	(1) Determination of the most likely limits of the capsule operational power profile in order to specify power subsystem requirements (2) Examination of various candidate systems for capsule power sources to determine: (a) What systems are available that can be made applicable to lander systems operations (b) Which power systems can be eliminated by recognition of obvious defects or deviations from lander requirements (c) Which system or systems are best suited for capsule applications based on the mission load profile, requirements and system characteristics
1971 lander science sample payload	Development of capsule science instrument requirements which would be typical of a 1971 lander; information on these requirements is needed to make the previous five study items meaningful. These requirements include: (1) Weight (2) Power (3) Volume (4) Data rates (5) Lifetime (6) Field of view (7) Atmospheric access (8) Radiation tolerance (9) Temperature tolerance Representative requirements that have been developed for the science payload are: (1) Atmospheric water vapor analysis (2) Atmospheric composition analysis (3) Ground gas analysis (4) Atmospheric pressure (5) Atmospheric temperature (6) Wind velocity

LAB B01468

UNCLASSIFIED [redacted]